

StainFuser: Controlling Diffusion for Faster Neural Style Transfer in Multi-Gigapixel Histology Images

Robert Jewsbury¹ (✉), Ruoyu Wang¹,
Abhir Bhalerao¹, Nasir Rajpoot^{1,2}, and Quoc Dang Vu^{1,2}

¹ Tissue Image Analytics Centre, University of Warwick

² Histofy, United Kingdom

{rob.jewsbury, ruoyu.wang.2, n.m.rajpoot}@warwick.ac.uk

Abstract. Stain normalization algorithms aim to transform the color and intensity characteristics of a source multi-gigapixel histology image to match those of a target image, mitigating inconsistencies in the appearance of stains used to highlight cellular components in the images. We propose a new approach, StainFuser, which treats this problem as a style transfer task using a novel Conditional Latent Diffusion architecture, eliminating the need for handcrafted color components. With this method, we curate SPI-2M the largest stain normalization dataset to date of over 2 million histology images with neural style transfer for high-quality transformations. Trained on this data, StainFuser outperforms current state-of-the-art GAN and handcrafted methods in terms of the quality of normalized images. Additionally, compared to existing approaches, it improves the performance of nuclei instance segmentation and classification models when used as a test time augmentation method on the challenging CoNIC dataset. Finally, we apply StainFuser on multi-gigapixel Whole Slide Images (WSIs) and demonstrate improved performance in terms of computational efficiency, image quality and consistency across tiles over current methods.

Keywords: Diffusion · Computational Pathology · Stain Normalisation

1 Introduction

In recent years, artificial intelligence (AI) algorithms have excelled in many tasks in the Computational Pathology (CPath) domain, such as tumor detection [13, 17], nuclei instance segmentation and classification [1, 10, 12, 49] and biomarker prediction [2, 18, 45]. However, as noted by [5, 16, 40, 43], real-life variations often occur during the data acquisition process of gigapixel histology images stained with Haematoxylin and Eosin. These variations, such as stain variance, scanner difference and tissue preparation, can greatly affect the AI algorithms’ performance in prognostic and diagnostic assessment of patients.

These alterations also pose great challenges for the decision-making of clinical practitioners [36]. Broadly speaking, these alterations can be considered as parts of the bigger domain shift problem in machine learning. Thus, addressing this problem is important for ensuring more consistent results in CPath algorithms and applications.

To address the color variations that occur due to staining and scanner variations, stain normalization is a common approach. At a high level, the aim is to make the color and intensity of a "source" image similar to another image, often termed the "target". Many CPath-specific, handcrafted, methods [24, 30, 42] have been proposed to separate and recombine the properties and intensities of stains based on their pre-defined chemical properties for capturing light, represented as stain matrices, to align the source image's colors with a desired target image's colors. A stain matrix thusly denotes densities of the stain chemicals within a tissue sample and their corresponding *RGB* values captured in the digital images.

GAN-based methods [4, 6, 35] have also been proposed to eliminate the need for these stain matrices. However, training GAN models can be difficult [4, 41] and thus easily lead to poor generation quality. Additionally, there exists little pairwise image data for training GAN models for stain normalization, many proposed algorithms [4, 6, 35] therefore resolve this by *training* their GAN models to reconstruct a *RGB* image from its grayscale counterpart. This approach results in models that are not directly transferable to different domains that exhibit stain properties unseen during training.

We approach the stain normalization problem as a style transfer task introducing a Conditional Latent Diffusion-based architecture for Stain Normalization, termed StainFuser. Recently, diffusion models have emerged as a superior method compared to GANs in both quality and training stability [7, 15, 28, 51]. To the best of our knowledge, this is the first study to employ diffusion models for stain normalization. To train StainFuser, we employ neural style transfer (NST) [9] to generate the transformed versions of each source and target image pair. This process generates a high-quality dataset and overcomes the paucity of data issue. Thus, we list our contributions as follows:

- We propose StainFuser, a novel method that does not require any handcrafted color components (i.e. stain properties) or other transformations and directly applies the style of the target image to the source image.
- We publish SPI-2M (Stylized Pathological Images), the largest dataset for stain normalization to date of over 2 million images³. We believe this will benefit other generative approaches for stain normalization other than StainFuser.
- We show that images generated by StainFuser can greatly enhance nuclei instance segmentation and classification models compared to handcrafted [30, 42] and GAN-based [6] methods.

³ Both our code and data will be available at: <https://github.com/R-J96/stainFuser>

- We conduct extensive ablation experiments to investigate the importance of components in our model both in terms of image quality, downstream performance and inference time.
- We demonstrate StainFuser’s quality on multi-gigapixel Whole Slide Images (WSIs), maintaining consistently high quality across tiles within a WSI.

2 Related Works

Reinhard *et al.* [27] introduced a technique for aligning the color distribution of a given image to a reference image in $L^*a^*b^*$ color space, which has found applications for stain normalization tasks. However, Reinhard *et al.* [27] was originally designed for generic color adjustment and was not specifically tailored for histology stain normalization. Subsequently, several prominent approaches in computational pathology, such as Ruifrok *et al.* [30], Macenko *et al.* [24] and Vahanade *et al.* [42] either proposed or leveraged the concept of the stain matrix to address the task of stain normalization for this research field.

In recent years, GAN-based approaches have emerged as alternatives to the aforementioned handcrafted methods, well-known methods include the works of Salehi *et al.* [35] and Cong *et al.* [6]. These works follow a vein established by Cho *et al.* [4]. In particular, due to the lack of pairwise data in stain normalization tasks, Cho *et al.* [4] trained their GAN models to reconstruct a *RGB* image from its grayscale counterpart. This grayscale transformation effectively merges diverse stains (or color styles) into a uniform color space [4], and could result in information loss despite employing additional operations [6]. Consequently, these models require retraining to adapt to any new target domain with new color distributions. In addition, GAN-based stain normalization models also face challenges in training, notably due to well-known issues such as mode collapse [41] and may need additional constraints for a stabilized generation quality [4].

Recently, denoising diffusion probabilistic models (DDPMs) [15, 38] have emerged as a new set of generative models for image synthesis. DDPMs are a collection of generative models that produce high-quality images through iterative denoising. In contrast to GANs, diffusion models exhibit more stable training and produce higher-quality images [15]. Furthermore, Rombach *et al.* [28] enhanced diffusion models’ speed and performance by introducing a latent diffusion model (LDM) that operates in variational autoencoder (VAE)-encoded latent space. In addition, the ability to incorporate various conditions (*e.g.*, texts, images, feature representations) into the diffusion models facilitates more applications such as text-to-image generation [28, 31, 34, 51], image super-resolution [8] or image editing [23]. However, the effectiveness of diffusion models in CPath tasks remains under-explored, with limited studies conducted [20, 50].

Furthermore, despite numerous new stain normalization methods, their effectiveness on the domain shift problem remains unassessed on a large scale. To the best of our knowledge, the work by Vu *et al.* [43], is the first major attempt to characterize the benefits of stain normalization to a downstream task across a diverse range of stain targets. Specifically, this includes ~ 200 targets distributed across the color space that typically envelopes CPath image data. Here,

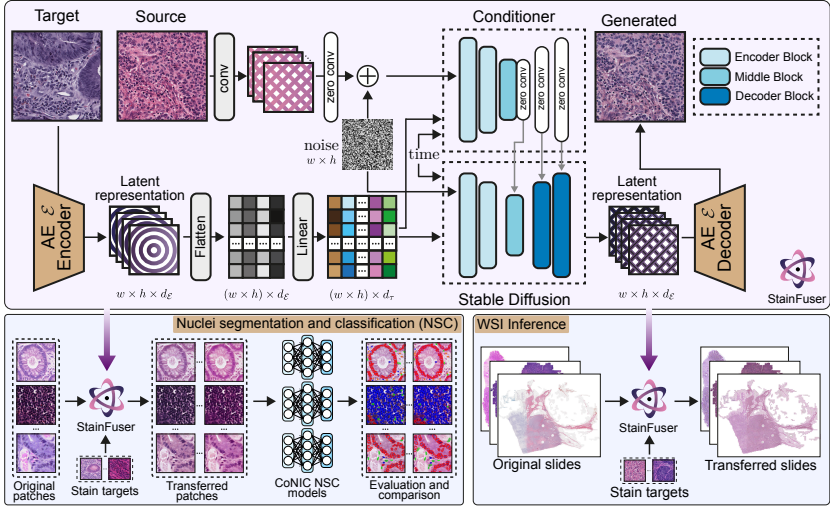


Fig. 1: The diagram of the proposed StainFuser. StainFuser takes in a source and target image to predict the stain normalized version of the source image. The application of StainFuser was demonstrated through a nuclei segmentation and classification task and a WSI-level inference task.

the authors compared the performance of Ruifork [30] and Vahadane [42] methods against the NST method [9]. They found NST provides the most consistent performance improvement for the nuclei instance segmentation and classification problem, a well-known difficult problem in CPath field [10], across all stain targets.

Thus, inspired by this observation, our paper explores the application of NST to generate pairwise images for training a generative model for stain normalization and explores the utilization of diffusion models for efficient and high-quality stain normalization.

3 Method

StainFuser aims to predict a neural style transferred version of an input source image given a target image as shown in Figure 1. As no public datasets of sufficient quality and quantity are available, we curate SPI-2M a pairwise stain normalization dataset from publicly available sources by applying NST to the sampled source and target pairs.

3.1 Creating SPI-2M

Here, we describe how we curate three distinct image patch sets: the source set $\mathbb{S} = \{p_1^s, p_2^s, \dots, p_n^s\}$ contains samples to be processed for stain normalization; the target set $\mathbb{T} = \{p_1^t, p_2^t, \dots, p_n^t\}$ where each sample ideally represents a unique

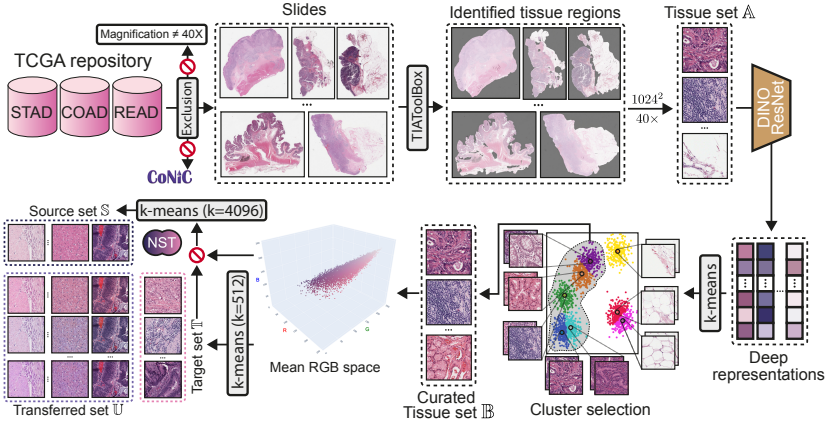


Fig. 2: Overview of the data curation workflow: Slides were sourced from the TCGA repository, followed by the patch extraction from identified tissue regions. A two-stage clustering pipeline was implemented to select biologically meaningful and representative patches, ensuring an accurate representation of the real-world morphology and color distribution.

stain variation from the real-world stain distribution; lastly, the transferred set \mathcal{U} is created by applying NST on \mathcal{S} and \mathcal{T} .

Slide selection. To comprehensively capture and include the real-world variations present in CPath, we retrieved slides from the public TCGA repository⁴. Since the CoNIC challenge dataset [10] was used as the evaluation dataset, to ensure the consistency of the tissue domain between the training and the evaluation datasets, 3 TCGA cohorts related to the gastrointestinal (GI) tract were selected for our analysis, namely TCGA-STAD (stomach), TCGA-COAD (colon) and TCGA-READ (rectal). Slides used in the CoNIC challenge were excluded. To curate high-quality samples, slides that lack magnification level information and slides scanned at less than $40\times$ magnification level were excluded. This results in a total of 686 slides scanned at $40\times$ magnification level for further analysis.

Patch selection. Tissue masks of the selected slides were generated using the TIAToolbox [25] to remove background, artifacts and pen marks. Subsequently, patches with the size of 1024^2 at $40\times$ magnification level were extracted from slides. We denote the patches extracted from these slides as dataset \mathcal{A} .

Source and target selection. To select representative patches that broadly reflect the diversity of tissue morphology and stains within image set \mathcal{A} , we implement a two-stage clustering pipeline, as shown in Figure 2. Inspired by [26,44], we extract biologically meaningful clusters by clustering the deep features of the image patches within \mathcal{A} .

⁴ <https://www.cancer.gov/tcga>

In the first stage, using ResNet-50 pretrained with DINO [3] on the ImageNet dataset [33], for each patch $p \in \mathbb{A}$, we obtain a set of deep feature vectors $Z = \{z_1, z_2, \dots, z_n\}$ from the images in tissue set \mathbb{A} . We then use k-means clustering to retrieve a set $C = \{c_1, c_2, \dots, c_{128}\}$ of 128 clusters from the feature set Z . Afterward, we visually examine the patches within each cluster to determine if that cluster contains unfit tissue components such as adipose tissues or more meaningful histological patterns (*i.e.* majorly containing known tissue patterns like glands or lymphoid aggregate). Subsequently, we remove all patches within the cluster we deem unfit from further consideration and denote the set containing the remaining valid image patches as set \mathbb{B} .

In the second stage, to select representative patches that reflect the staining style (*i.e.* the color), instead of using deep features to represent each patch as in the first stage, we represent each patch within \mathbb{B} by their mean RGB value \hat{z} and obtain $\hat{Z} = \{\hat{z}_1, \hat{z}_2, \dots, \hat{z}_n\}$.

For curating the target set \mathbb{T} , we perform k-means clustering on \hat{Z} and obtain a set of 512 clusters $\hat{C} = \{\hat{c}_1, \hat{c}_2, \dots, \hat{c}_{512}\}$. To select the most representative patch of each cluster, we select *one single patch* within \mathbb{B} which is the closest to its cluster center in \hat{C} in terms of the Euclidean distance in the RGB color space.

On the other hand, for curating the source set \mathbb{S} , we first obtain a subset $\bar{\mathbb{B}} = \{p \in \mathbb{B} : p \notin \mathbb{T}\}$ before performing the same clustering and the patch selection. Here, we extract 4096 clusters and similarly select *one single patch* within $\bar{\mathbb{B}}$ to represent each cluster.

In summary, from \mathbb{A} , we obtained the source tissue set \mathbb{S} which contains 4096 images and the target tissue set \mathbb{T} which contains 512 images that are evenly spaced in the color space of \mathbb{A} (*i.e.* TCGA-STAD, TCGA-COAD and TCGA-READ).

Generating the transferred set. Finally, we apply NST on each pairwise combination of image patches in \mathbb{S} and \mathbb{T} . Through this process, for a given pair p^s, p^t we obtain image $p_{s,t}^u = NST(p^s, p^t)$ whose tissue components are the same as p^s but have their color based on the stain of similar tissue morphology observed in p^t . This process results in 2,097,152 style transferred images in the transferred set \mathbb{U} . Specifics on how NST are setup and utilized in our work are provided in the supplementary materials A1.

3.2 StainFuser for stain normalization.

Consider a source image patch p^s from the source set \mathbb{S} , and a target-stain image patch p^t from the target set \mathbb{T} . In our proposed diffusion framework, StainFuser, as illustrated in Figure 1, the model takes p^s and p^t as inputs. The StainFuser retains the structural and morphological characteristics of p^s while applying the stain characteristics of p^t to p^s , resulting in a transferred sample $p_{s,t}^u$ belonging to the transferred set \mathbb{U} .

To control the Stable Diffusion backbone to incorporate the stain characteristics of p^t into the generated image $p_{s,t}^u$, we adopt the cross-attention mechanism as applied in Rombach *et al.* [28]. Given a stain target image p^t , a latent representation is generated using an AutoEncoder (AE) \mathcal{E} , resulting in

$\mathcal{E}(p^t) \in \mathbb{R}^{w \times h \times d_{\mathcal{E}}}$, where $d_{\mathcal{E}}$ is the feature-length of the AE \mathcal{E} . $\mathcal{E}(p^t)$ is then flattened to $\mathcal{E}'(p^t) \in \mathbb{R}^{(w \times h) \times d_{\mathcal{E}}}$. To match the feature length d_{τ} of the encoder τ_{θ} used in a pre-trained Stable Diffusion model, $\mathcal{E}'(p^t)$ is projected to $l(\mathcal{E}'(p^t)) \in \mathbb{R}^{(w \times h) \times d_{\tau}}$ through a linear projection $l(\cdot)$. Then $l(\mathcal{E}'(p^t))$ is incorporated into the UNet backbone of the diffusion model through cross-attention layers defined as follows,

$$\text{Attention}(Q, K, V) := \text{softmax}\left(\frac{QK^T}{\sqrt{d}}\right) \cdot V, \quad (1)$$

where $Q = W_Q^{(i)} \cdot \varphi_i(z_t)$, $K = W_K^{(i)} \cdot l(\mathcal{E}'(p^t))$ and $V = W_V^{(i)} \cdot l(\mathcal{E}'(p^t))$. Here, $\varphi_i(z_t)$ denotes an intermediate output of the UNet, and z_t denotes the noised version of $z_0 = \mathcal{E}(p_{s,t}^u)$ at timestep t .

To further control the Stable Diffusion for generating the $p_{s,t}^u$ which adhere to the structure of the source image p^s , we incorporate the p^s into the Stable Diffusion model using zero convolution layers, following the approach proposed in Zhang *et al.* [51]. The source image p^s is firstly encoded by a learnable network h to match the spatial resolution of the AE-encoded input samples. For a pretrained block $\mathcal{F}(\cdot; \Theta)$ from the Stable Diffusion, a trainable copy of \mathcal{F} is created, which we denote as $\mathcal{F}(\cdot; \Theta_c)$, as shown in Figure 1. The original $\mathcal{F}(\cdot; \Theta)$ is frozen. $\mathcal{F}(\cdot; \Theta_c)$ takes the encoding $h(p^s)$ of the source image, and incorporates its output into the original block through zero convolution layers, defined as follows,

$$y_c = \mathcal{F}(x; \Theta) + \mathcal{F}_0(\mathcal{F}(x + \mathcal{F}_0(h(p^s); \Theta_{z1}); \Theta_c); \Theta_{z2}), \quad (2)$$

where $\mathcal{F}_0(\cdot; \cdot)$ is the zero convolution layers with weights and bias initialized to zero. $\mathcal{F}_0(\cdot; \Theta_{z1})$ and $\mathcal{F}_0(\cdot; \Theta_{z2})$ are two instances of zero convolution layers which takes the source encoding $h(p^s)$ and the trainable copy's outputs respectively. As shown in Figure 1, the Conditioner receives the timestep t , encoded target-stain image $l(\mathcal{E}'(p^t))$, and the concatenated source image with the noise vector; generates intermediates representations and then provide these to the Stable Diffusion model through a set of zero convolution layers. We defer to supplementary material A.2 the detailed definitions of the latent diffusion models.

The learning objective of StainFuser is defined as:

$$\mathcal{L} = \mathbb{E}_{z_0^u, t, p^s, p^t, \epsilon \sim \mathcal{N}(0,1)} \left[\|\epsilon - \epsilon_{\theta}(z_t^u, t, p^s, p^t)\|_2^2 \right], \quad (3)$$

where z_0^u and z_t^u are latent representations of the transferred variable $p_{s,t}^u$ at timestep 0 and t , respectively; ϵ is the noise term sampled from a Gaussian distribution to be input into the diffusion model; $\epsilon_{\theta}(\cdot)$ is the estimated noise term by the diffusion model parameterized by θ , given the sample z_t^u , timestep t , conditions p^s and p^t .

4 Experiments

In our experiments, we compare StainFuser with two traditional stain normalization methods (Ruifrok [30] and Vahadane [42]), a GAN-based method

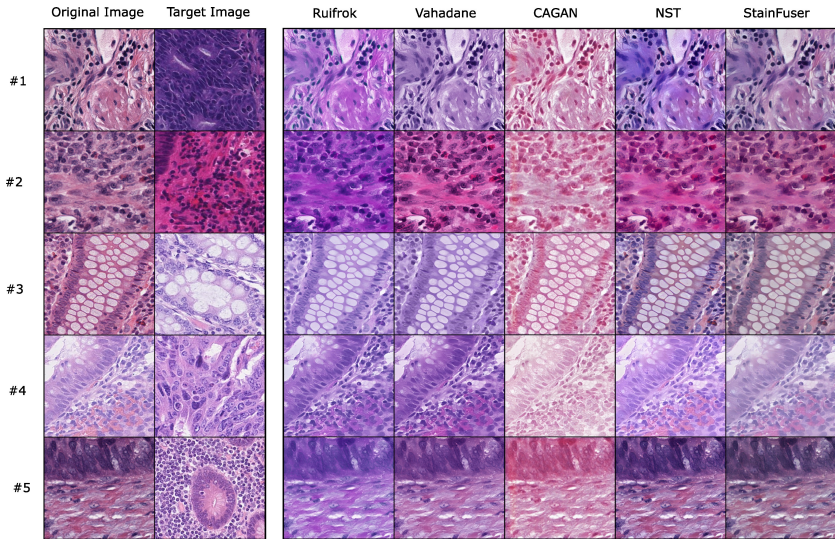


Fig. 3: Qualitative comparisons between StainFuser and other methods on CoNIC test set examples. All inference was performed at 512^2 resolution and then resized for display purposes. Only StainFuser and NST preserve the color contrast between important tissue components such as stroma, glands, lumen and blood vessels present in the original image.

(CAGAN [6]) and NST [9] itself in terms of image quality and downstream performance for nuclei instance segmentation and classification on the CoNIC dataset [11]. We perform extensive ablations of the training and inference hyperparameters including qualitative results. Finally, we also present results applying the methods for WSI inference showcasing the clinical applications of StainFuser and detail the limitations of our approach. Training details such as hyperparameters and other observations can be found in the model training Section B of the supplementary materials.

Evaluation Dataset We trained our StainFuser models based on the curated dataset as described in Section 3.1. To evaluate our models, we utilized the data from the CoNIC challenge [11]. This dataset consists of H&E stained image tiles from colorectal cancer WSIs, there are 5k training images with 431,913 unique nuclei instances and 1k testing images with 103,150 nuclei instances. Each image is annotated with panoptic segmentation labels of 6 nuclei classes, neutrophils, epithelial cells, lymphocytes, plasma cells, eosinophils and connective cells in addition to the background. As noted in Section 3.1, the curated data for training our proposed StainFuser does not include any examples within the CoNIC data.

Experimental Settings. Inspired by Vu *et al.* [43], we followed the same setup for evaluation on CoNIC for both image quality and downstream analysis. Specifically, to compare against the reported results of Ruifrok [30], Vahadane [42] and NST [9], we first used StainFuser to generate 101 versions of the test set altered with respect to the same target images as Vu *et al.* [43]. Additionally,

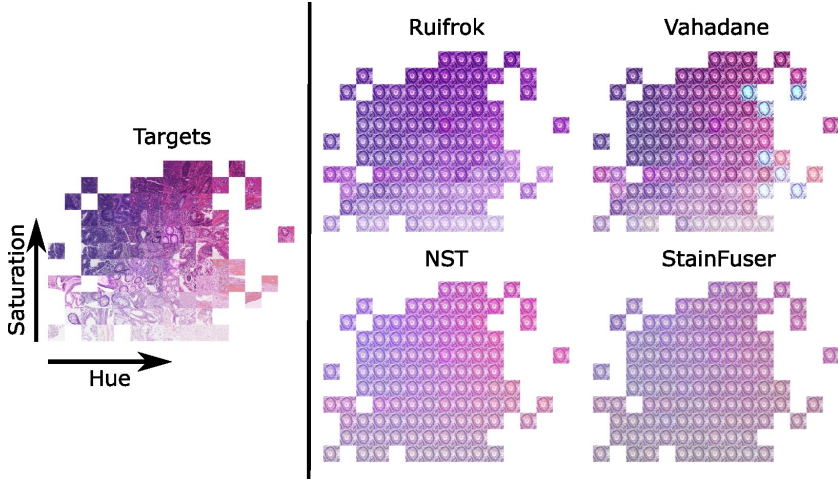


Fig. 4: Target images selected by sampling in HSV space and a test sample normalised by each method assessed. Targets are displayed on 2D plane where x-axis is Hue and y-axis is Saturation by the mean value of the respective target’s Hue and Saturation. High-resolution versions of each set of images are included in the Additional Illustrative Results Section F of the supplementary material.

we also compared against the published CAGAN method [6] trained on TCGA-IDH [21]. We utilised the nuclei instance segmentation and classification task in CoNIC [11] for downstream evaluation as we consider one of the most important aspects of a stain normalization method’s utility is its effect on model performance in downstream tasks. Please see the extended experiment design Section C in the supplementary materials for further motivation of this setup, full methodological details are described in Vu *et al.* [43].

We assess the performance of three state-of-the-art (SoTA) methods from the CoNIC challenge, namely *Pathology AI* (PathAI) [52], *MDC Berlin | IFP Bern* (Bern) [32] and *EPFL | StarDist* (StarDist) [48] on each stain normalized test set individually, to evaluate and compare StainFuser across model architectures as well as target images for this challenging downstream task. For evaluating the model performance, we utilized mPQ^+AUC as described in [43]. Where possible, we also report the mean $mPQ^+AUC \pm$ the standard deviation of a model’s downstream performance across the entire distribution of altered test sets.

4.1 Evaluating Image Appearance - Qualitative

At the micro level, Figure 3 shows that Ruifrok [30] produces very purple images regardless of the chosen target. On the other hand, while Vahadane does not suffer from this issue, it fails to differentiate the color of distinct cellular components. For instance, in #3, the inner portion of the gland is also colored purple. The worst of all is CAGAN [6] where it can not utilize the target images and can only map to a single domain (rose red). Unlike these, StainFuser and

Table 1: Image quality comparisons with the SoTA methods on the CoNIC test set. All results are reported for 512² images. Inference time is reported per image, Ruifrok and Vahadane times were computed on an Intel Xeon Gold 6240 CPU multiprocessing 32 images simultaneously; NST, CAGAN and StainFuser were all computed on an A100 GPU with a batch size of 32 for CAGAN and StainFuser. All times were calculated over a full test set of 1000 images, the time per batch of 32 images was recorded and then averaged and reported along with the standard deviation across batches. Best results are shown in **blue**

Method	Inference time (s)	FID↓	PSNR↑	SSIM↑
Ruifrok [30]	0.215 ± 0.017	34.261 ± 4.848	14.395 ± 1.298	0.855 ± 0.039
Vahadane [42]	0.518 ± 0.051	37.010 ± 18.393	14.363 ± 1.435	0.844 ± 0.063
CAGAN [6]	0.021 ± 0.006	119.789	16.653	0.847
NST [9]	12.404 ± 1.184	22.210 ± 8.561	24.937 ± 3.202	0.931 ± 0.020
StainFuser	0.413 ± 0.005	25.882 ± 8.233	23.911 ± 0.816	0.875 ± 0.010

NST produce images that maintain good contrast between important cellular components, such as the stroma and lumen as in #3. Compared to NST, visually, StainFuser produces more color-consistent images but its colors are less vibrant, as seen in #1.

At the macro level, following Vu et al. [43], we used images from the CoNIC dataset that are evenly spaced the HSV colorspace as target images, as shown in Figure 4. By normalizing a sample image using these chosen targets, we can evaluate how each normalization method performs across a typical colorspace of CPath data. From Figure 4, we see that Vahadane has many irregular outputs, such as the orange outputs and very pale images produced in the bottom row. Ruifrok is consistent in terms of output color, which is predominantly purple; however, it struggles when very pale, light images are used as the target (bottom region of the plot). NST and StainFuser however, produce more consistent normalized images across the evaluated color range. Compared to StainFuser, NST produces more vibrant images in general.

Overall, our results in Figure 3 and Figure 4 demonstrate that StainFuser has comparable performance against NST and is superior to other methods. It also is capable of producing images that are color-consistent with a highly varied range of target images, unlike handcrafted methods such as Ruifrok and Vahadane normalization.

4.2 Evaluating Image Appearance - Quantitative

Following traditional approaches for evaluating generative models, we compute the Fréchet Inception Distance (FID) [14], Peak Signal to Noise Ratio (PSNR) and Structural Similarity Index Measure (SSIM) [47] for the generated test set(s) and compare them against original images from CoNIC. Our results are detailed in Table 1 along with inference time comparisons. We find StainFuser outperforms Ruifrok, Vahadane and CAGAN in terms of FID, PSNR and SSIM. While NST has superior image quality, StainFuser is competitive and substantially faster achieving a 30× speed up in inference time.

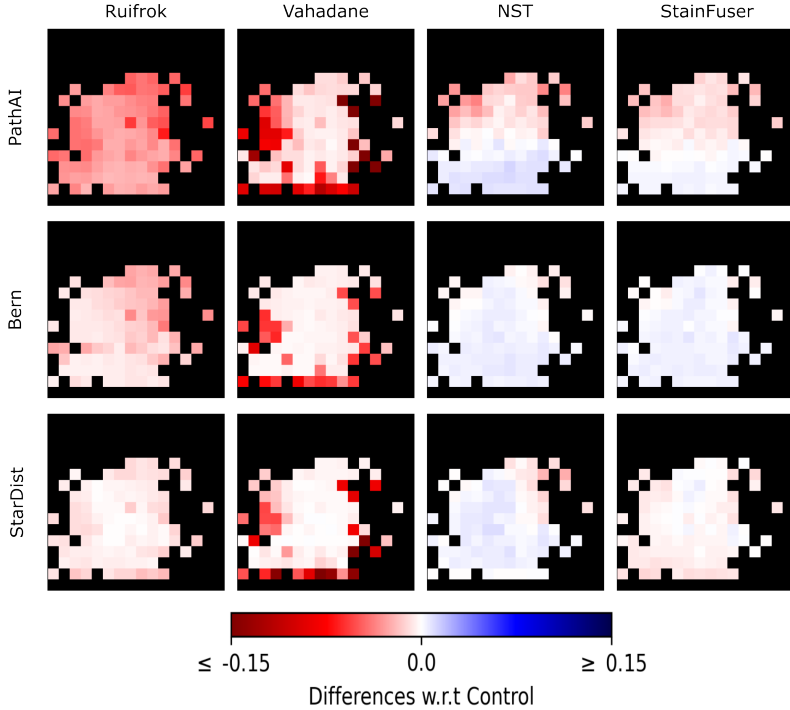


Fig. 5: Heatmaps of the difference in the mPQ^+AUC between the **Control** and the test set where its color was shifted w.r.t each sampled target. Changes in performance are displayed in the same pattern as their corresponding target in Figure 4. CAGAN is excluded as it can not normalize w.r.t. a specific target image.

4.3 Downstream Evaluations

We report our results in Table 2. Similar to Section 4.1, we observe that StainFuser consistently outperforms Ruifrok, Vahadane and CAGAN for all models and all metrics. Interestingly, compared to NST (*i.e.* the ground truth for training StainFuser), StainFuser outperforms NST in terms of mPQ^+AUC as well as the original data when using the Bern model. On the other hand, for both PathAI and StarDist, NST is better than StainFuser in terms of mDQ^+AUC and mPQ^+AUC . We include qualitative examples of each model’s performance with each normalization method in Section F of the supplementary material.

Our results thus show that different model architectures and training strategies respond differently to various normalization methods at inference time. Additionally, the superiority of NST and StainFuser compared to other methods in image quality and consistency also is reflected in the downstream evaluation. This is evidenced by a clear gap in performance across the board between NST and StainFuser and other methods as well as how close NST and StainFuser are to the performance of the original setup.

Results per target. To explore how model performance varied by normalization target across methods we display the individual results from Table 2 as a set of heatmaps in Figure 5. Each square cell is located at the corresponding position of the target in HSV space from Figure 4. The color of each cell denotes the relative performance in terms of mPQ^+AUC of a given model compared with the model’s performance on the **Control** set. Full details of the **Control** set can be found in the Section C of the supplementary material. We can see that StainFuser is competitive with NST and both significantly outperform Ruifrok and Vahadane normalisation. With Ruifrok and Vahadane at best a given model performs on par with the un-normalised data and more often than not performs worse. Vahadane in particular with pale images, in the bottom row, and other outliers results in significantly worse performance. By contrast, NST and StainFuser improve every model’s performance, particularly PathAI and Bern, for a multitude of targets. With the Bern model we see StainFuser improves performance for almost all sampled targets reinforcing prior findings that Bern is most robust to variations in color and compression [43].

With PathAI and StarDist, we observe NST and StainFuser have very different patterns. By cross-referencing Figure 5 against Figure 4, we observe that for target images with low saturation (lower region on the y-axis), PathAI performs better with StainFuser whereas it is the opposite with StarDist.

It is unknown to us what leads to such a significant divergence in the performance patterns. However, we speculate that different training augmentation regimes, while vastly increasing the original training data, also inadvertently and intractably diverge the data distribution observed by the models. Together with the inherent capacity of each model architecture in capturing such distribution, we ended up with each final model having widely different color foci for good performance.

4.4 Ablation Studies

We study how various components of the training strategy affect final performance and explore the tradeoff between the number of denoising steps and generated image quality at inference time. For all downstream analysis in our ablations, we use PathAI’s model. See Section D of the supplementary materials for full details of our ablation analyses.

Number of Denoising steps. We perform inference across all test sets with different numbers of denoising steps and analyse the impact this has on image quality and downstream model performance and report the results in Table 3. Here, we see FID, PSNR and SSIM change by -10.092 FID, +2.812 PSNR and +0.015 SSIM between 5 and 100 denoising steps. However, there are diminishing returns when the number of denoising steps increases beyond 10. Due to the results of this ablation, we used 20 denoising steps for all other downstream analyses as this represented the best compromise between inference time, image quality and downstream performance.

Table 2: Comparison with other Stain Normalisation methods as a test-time augmentation on the CoNIC test set. Results are the mean \pm standard deviation across all 101 target sets except for the Original data and CAGAN as there was no distribution of results for these. The best-performing stain normalisation method is highlighted in blue.

Model	Method	$mDQ^+ AUC \uparrow$	$mSQ^+ AUC \uparrow$	$mPQ^+ AUC \uparrow$
PathAI	Original	0.293	0.374	0.220
	Ruifrok [30]	0.248 ± 0.012	0.374 ± 0.002	0.186 ± 0.010
	Vahadane [42]	0.240 ± 0.069	0.368 ± 0.015	0.179 ± 0.052
	CAGAN [6]	0.163	0.366	0.121
	NST [9]	0.287 ± 0.016	0.375 ± 0.001	0.215 ± 0.012
	StainFuser	0.283 ± 0.010	0.378 ± 0.001	0.211 ± 0.007
Bern	Original	0.292	0.381	0.223
	Ruifrok [30]	0.275 ± 0.010	0.379 ± 0.003	0.209 ± 0.009
	Vahadane [42]	0.268 ± 0.031	0.380 ± 0.004	0.205 ± 0.024
	CAGAN [6]	0.187	0.379	0.143
	NST [9]	0.294 ± 0.004	0.382 ± 0.001	0.225 ± 0.004
	StainFuser	0.294 ± 0.003	0.392 ± 0.001	0.225 ± 0.003
StarDist	Original	0.281	0.381	0.215
	Ruifrok [30]	0.271 ± 0.006	0.382 ± 0.002	0.208 ± 0.004
	Vahadane [42]	0.249 ± 0.054	0.380 ± 0.004	0.191 ± 0.041
	CAGAN [6]	0.189	0.387	0.149
	NST [9]	0.280 ± 0.008	0.384 ± 0.001	0.216 ± 0.006
	StainFuser	0.274 ± 0.005	0.392 ± 0.001	0.211 ± 0.004

Table 3: Effect of denoising step number. Rows show performance across entire 101 target sets, $mPQ^+ AUC$ is using PathAI model on the CoNIC test sets. Image quality improves rapidly from 5 to 10 denoising steps and then starts to plateau.

Steps	Inference time (s)	$mPQ^+ AUC \uparrow$	FID \uparrow	PSNR \uparrow	SSIM \uparrow
5	0.146 ± 0.002	0.213 ± 0.011	42.150 ± 12.086	21.298 ± 0.704	0.853 ± 0.017
10	0.249 ± 0.003	0.214 ± 0.011	34.393 ± 10.680	23.148 ± 0.965	0.865 ± 0.017
20	0.408 ± 0.002	0.214 ± 0.011	32.760 ± 10.398	23.777 ± 1.090	0.868 ± 0.017
50	0.880 ± 0.003	0.214 ± 0.011	32.211 ± 10.292	24.034 ± 1.151	0.868 ± 0.018
100	1.713 ± 0.237	0.213 ± 0.011	32.058 ± 10.268	24.110 ± 1.166	0.868 ± 0.018

4.5 Inference on Whole Slide Images

We further qualitatively compare StainFuser against Vahadane and CAGAN at WSI-level in Figure 6. The technical details and more results are provided in Section F, Fig. A4, A5 of the supplementary materials. As can be seen from Figure 6, StainFuser shows a more consistent performance across the entire slide, whereas Vahadane’s varies significantly. This can be observed in **ROI#3** when using **Target#1** and **Target#2**. On the macro scale, Vahadane can also fail in certain regions and generate highly distorted images (*i.e.* the blueish color patches), as shown in **ROI#1**. Meanwhile, StainFuser’s result generally appears less vibrant than Vahadane’s, as demonstrated by **ROI#2**. Despite this, from the same region, StainFuser still managed to achieve a clearer distinction

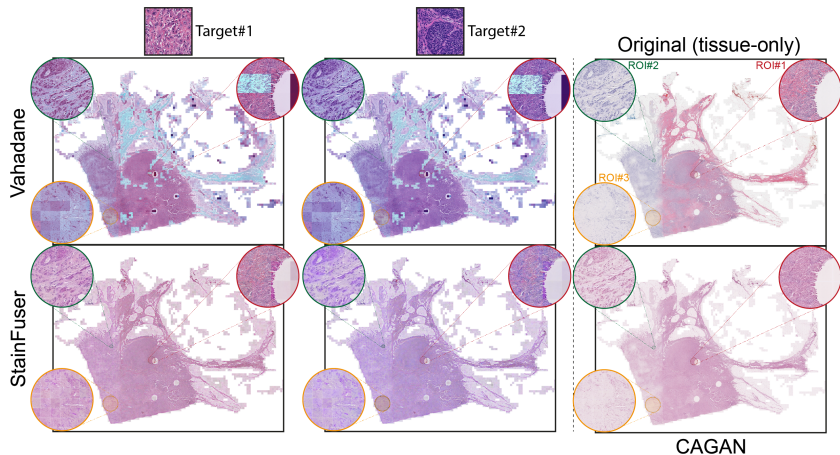


Fig. 6: WSI inference comparison between Vahadane, StainFuser and CAGAN. The slide was chosen from a different anatomic site (*i.e.* breast) and 2 target images were chosen from 2 different slides previously unseen by the StainFuser.

between the tumor and the stroma compared to Vahadane. In comparison to Vahadane and StainFuser, although CAGAN transforms the input image only to one particular color domain, visually it has better consistency for this particular sample. However, as noted previously, the finer details of the image are significantly compromised. We illustrate this issue in Fig. A5 in the supplementary materials.

4.6 Limitations

While StainFuser generates high-quality images with clear contrast between important tissue components, we identify the following limitations in our work. First, the StableDiffusion backbone is GPU memory intensive both for training and inference. Furthermore, the data curation we explored, while comprehensive, is restricted to three organs and does not represent the entire spectrum of tissue staining and morphologies possible. Additionally, curating data using NST is expensive, costing us over 10 thousand GPU hours. Finally, our method can sometimes produce slightly desaturated, less vibrant images compared to other approaches. While we’ve demonstrated this does not lead to worse image quality or downstream performance it is unclear what is causing this qualitative defect.

5 Conclusion

We present StainFuser, a novel method for stain normalization based on conditional diffusion models. For our approach, we curated to our knowledge the first, large-scale stain normalization dataset of over two million images. When trained on this dataset StainFuser achieves superior results compared to existing handcrafted and GAN-based methods in terms of image quality and downstream

performance on the challenging CoNIC dataset. In addition, our design achieves substantially better performance when used for WSI inference with superior color consistency between adjacent tiles and variations in stain compared to other methods. We believe our work provides a different perspective on the stain normalization task and the application of diffusion models in CPath.

References

1. Bashir, R.M.S., Qaiser, T., Raza, S.E.A., Rajpoot, N.M.: Hydramix-net: A deep multi-task semi-supervised learning approach for cell detection and classification. In: Interpretable and Annotation-Efficient Learning for Medical Image Computing: Third International Workshop, iMIMIC 2020, Second International Workshop, MIL3ID 2020, and 5th International Workshop, LABELS 2020, Held in Conjunction with MICCAI 2020, Lima, Peru, October 4–8, 2020, Proceedings 3. pp. 164–171. Springer (2020)
2. Bashir, R.M.S., Shephard, A.J., Mahmood, H., Azarmehr, N., Raza, S.E.A., Khurram, S.A., Rajpoot, N.M.: A digital score of peri-epithelial lymphocytic activity predicts malignant transformation in oral epithelial dysplasia. *The Journal of Pathology* (2023)
3. Caron, M., Touvron, H., Misra, I., Jégou, H., Mairal, J., Bojanowski, P., Joulin, A.: Emerging properties in self-supervised vision transformers. In: Proceedings of the IEEE/CVF international conference on computer vision. pp. 9650–9660 (2021)
4. Cho, H., Lim, S., Choi, G., Min, H.: Neural stain-style transfer learning using gan for histopathological images. arXiv preprint arXiv:1710.08543 (2017)
5. Ciompi, F., Geessink, O., Bejnordi, B.E., De Souza, G.S., Baidoshvili, A., Litjens, G., Van Ginneken, B., Nagtegaal, I., Van Der Laak, J.: The importance of stain normalization in colorectal tissue classification with convolutional networks. In: 2017 IEEE 14th International Symposium on Biomedical Imaging (ISBI 2017). pp. 160–163. IEEE (2017)
6. Cong, C., Liu, S., Di Ieva, A., Pagnucco, M., Berkovsky, S., Song, Y.: Colour adaptive generative networks for stain normalisation of histopathology images. *Medical Image Analysis* **82**, 102580 (2022)
7. Dhariwal, P., Nichol, A.: Diffusion models beat gans on image synthesis. *Advances in neural information processing systems* **34**, 8780–8794 (2021)
8. Gao, S., Liu, X., Zeng, B., Xu, S., Li, Y., Luo, X., Liu, J., Zhen, X., Zhang, B.: Implicit diffusion models for continuous super-resolution. In: Proceedings of the IEEE/CVF Conference on Computer Vision and Pattern Recognition. pp. 10021–10030 (2023)
9. Gatys, L.A., Ecker, A.S., Bethge, M.: A neural algorithm of artistic style. arXiv preprint arXiv:1508.06576 (2015)
10. Graham, S., Jahanifar, M., Vu, Q.D., Hadjigeorgiou, G., Leech, T., Snead, D., Raza, S.E.A., Minhas, F., Rajpoot, N.: Conic: Colon nuclei identification and counting challenge 2022 (2021)
11. Graham, S., Vu, Q.D., Jahanifar, M., Weigert, M., Schmidt, U., Zhang, W., Zhang, J., Yang, S., Xiang, J.P., Wang, X., Rumberger, J.L., Baumann, E., Hirsch, P., Liu, L., Hong, C., Avilés-Rivero, A.I., Jain, A., Ahn, H., Hong, Y., Azzuni, H., Xu, M., Yaqub, M., Blache, M.C., Pi’egu, B., Vernay, B., Scherr, T., Bohland, M., Löffler, K.U., Li, J., Ying, W., Wang, C., Kainmueller, D., Schonlieb, C.B., Liu, S., Talsania, D., Meda, Y., Mishra, P.K., Ridzuan, M., Neumann, O., Schilling, M.P.,

- Reischl, M., Mikut, R., Huang, B., Chien, H.C., Wang, C.P., Lee, C.Y., Lin, H., Liu, Z., Pan, X., Han, C., Cheng, J., Dawood, M., Deshpande, S., Bashir, R.M.S., Shephard, A.J., Costa, P., Nunes, J.D., Campilho, A.J.C., dos Santos Cardoso, J., HrishikeshP., S., Puthussery, D., DevikaR, G., JijiC., V., Zhang, Y., Fang, Z., Lin, Z., Zhang, Y., xin Lin, C., Zhang, L., Mao, L., Wu, M., Vo, V., Kim, S.H., Lee, T.H., Kondo, S., Kasai, S., Dumbhare, P., Phuse, V., Dubey, Y., Jamthikar, A.D., Vuong, T.T.L., Kwak, J.T., Ziaei, D., Jung, H., Miao, T., Snead, D.R.J., Raza, S.E.A., Minhas, F.A., Rajpoot, N.M.: Conic challenge: Pushing the frontiers of nuclear detection, segmentation, classification and counting. *Medical image analysis* **92**, 103047 (2023)
12. Graham, S., Vu, Q.D., Raza, S.E.A., Azam, A., Tsang, Y.W., Kwak, J.T., Rajpoot, N.: Hover-net: Simultaneous segmentation and classification of nuclei in multi-tissue histology images. *Medical image analysis* **58**, 101563 (2019)
 13. Gunesli, G.N., Bilal, M., Raza, S.E.A., Rajpoot, N.M.: A federated learning approach to tumor detection in colon histology images. *Journal of Medical Systems* **47**(1), 99 (2023)
 14. Heusel, M., Ramsauer, H., Unterthiner, T., Nessler, B., Hochreiter, S.: Gans trained by a two time-scale update rule converge to a local nash equilibrium. In: *Neural Information Processing Systems* (2017)
 15. Ho, J., Jain, A., Abbeel, P.: Denoising diffusion probabilistic models. *Advances in neural information processing systems* **33**, 6840–6851 (2020)
 16. Jahanifar, M., Raza, M., Xu, K., Vuong, T.T.L., Jewsbury, R., Shephard, A.J., Zamanitajeddin, N., Kwak, J.T., Raza, S.E.A., Minhas, F., Rajpoot, N.M.: Domain generalization in computational pathology: Survey and guidelines. *ArXiv abs/2310.19656* (2023)
 17. Jewsbury, R., Bhalerao, A., Rajpoot, N.M.: A quadtree image representation for computational pathology. 2021 IEEE/CVF International Conference on Computer Vision Workshops (ICCVW) pp. 648–656 (2021)
 18. Kather, J.N., Pearson, A.T., Halama, N., Jäger, D., Krause, J., Loosen, S.H., Marx, A., Boor, P., Tacke, F., Neumann, U.P., et al.: Deep learning can predict microsatellite instability directly from histology in gastrointestinal cancer. *Nature medicine* **25**(7), 1054–1056 (2019)
 19. Kingma, D.P., Ba, J.: Adam: A method for stochastic optimization. *CoRR abs/1412.6980* (2014)
 20. Linmans, J., Raya, G., van der Laak, J., Litjens, G.: Diffusion models for out-of-distribution detection in digital pathology. *Medical Image Analysis* p. 103088 (2024)
 21. Liu, S., Shah, Z., Sav, A., Russo, C., Berkovsky, S., Qian, Y., Coiera, E., Di Ieva, A.: Isocitrate dehydrogenase (idh) status prediction in histopathology images of gliomas using deep learning. *Scientific reports* **10**(1), 7733 (2020)
 22. Loshchilov, I., Hutter, F.: Decoupled weight decay regularization. In: *International Conference on Learning Representations* (2019)
 23. Lugmayr, A., Danelljan, M., Romero, A., Yu, F., Timofte, R., Van Gool, L.: Repaint: Inpainting using denoising diffusion probabilistic models. In: *Proceedings of the IEEE/CVF Conference on Computer Vision and Pattern Recognition*. pp. 11461–11471 (2022)
 24. Macenko, M., Niethammer, M., Marron, J.S., Borland, D., Woosley, J.T., Guan, X., Schmitt, C., Thomas, N.E.: A method for normalizing histology slides for quantitative analysis. In: *2009 IEEE international symposium on biomedical imaging: from nano to macro*. pp. 1107–1110. IEEE (2009)

25. Pocock, J., Graham, S., Vu, Q.D., Jahanifar, M., Deshpande, S., Hadjigeorgiou, G., Shephard, A., Bashir, R.M.S., Bilal, M., Lu, W., et al.: Tiatoolbox as an end-to-end library for advanced tissue image analytics. *Communications medicine* **2**(1), 120 (2022)
26. Quiros, A.C., Coudray, N., Yeaton, A., Yang, X., Liu, B., Le, H., Chiriboga, L., Karimkhan, A., Narula, N., Moore, D.A., Park, C.Y., Pass, H., Moreira, A.L., Quesne, J.L., Tsirigos, A., Yuan, K.: Mapping the landscape of histomorphological cancer phenotypes using self-supervised learning on unlabeled, unannotated pathology slides (2023)
27. Reinhard, E., Adhikmin, M., Gooch, B., Shirley, P.: Color transfer between images. *IEEE Computer graphics and applications* **21**(5), 34–41 (2001)
28. Rombach, R., Blattmann, A., Lorenz, D., Esser, P., Ommer, B.: High-resolution image synthesis with latent diffusion models. In: *Proceedings of the IEEE/CVF conference on computer vision and pattern recognition*. pp. 10684–10695 (2022)
29. Ronneberger, O., Fischer, P., Brox, T.: Convolutional networks for biomedical image segmentation. In: *Medical Image Computing and Computer-Assisted Intervention—MICCAI 2015 Conference Proceedings* (2022)
30. Ruifrok, A.C., Johnston, D.A., et al.: Quantification of histochemical staining by color deconvolution. *Analytical and quantitative cytology and histology* **23**(4), 291–299 (2001)
31. Ruiz, N., Li, Y., Jampani, V., Pritch, Y., Rubinstein, M., Aberman, K.: Dream-booth: Fine tuning text-to-image diffusion models for subject-driven generation. In: *Proceedings of the IEEE/CVF Conference on Computer Vision and Pattern Recognition (CVPR)*. pp. 22500–22510 (June 2023)
32. Rumberger, J.L., Baumann, E., Hirsch, P., Kainmueller, D.: Panoptic segmentation with highly imbalanced semantic labels. *2022 IEEE International Symposium on Biomedical Imaging Challenges (ISBIC)* pp. 1–4 (2022)
33. Russakovsky, O., Deng, J., Su, H., Krause, J., Satheesh, S., Ma, S., Huang, Z., Karpathy, A., Khosla, A., Bernstein, M., et al.: Imagenet large scale visual recognition challenge. *International journal of computer vision* **115**, 211–252 (2015)
34. Saharia, C., Chan, W., Saxena, S., Li, L., Whang, J., Denton, E.L., Ghasemipour, K., Gontijo Lopes, R., Karagol Ayan, B., Salimans, T., Ho, J., Fleet, D.J., Norouzi, M.: Photorealistic text-to-image diffusion models with deep language understanding. In: Koyejo, S., Mohamed, S., Agarwal, A., Belgrave, D., Cho, K., Oh, A. (eds.) *Advances in Neural Information Processing Systems*. vol. 35, pp. 36479–36494. Curran Associates, Inc. (2022)
35. Salehi, P., Chalechale, A.: Pix2pix-based stain-to-stain translation: A solution for robust stain normalization in histopathology images analysis. In: *2020 International Conference on Machine Vision and Image Processing (MVIP)*. pp. 1–7. IEEE (2020)
36. Salvi, M., Caputo, A., Balmativola, D., Scotto, M., Pennisi, O., Michielli, N., Mogetta, A., Molinari, F., Fraggetta, F.: Impact of stain normalization on pathologist assessment of prostate cancer: A comparative study. *Cancers* **15**(5), 1503 (2023)
37. Schuhmann, C., Beaumont, R., Vencu, R., Gordon, C.W., Wightman, R., Cherti, M., Coombes, T., Katta, A., Mullis, C., Wortsman, M., Schramowski, P., Kundurthy, S.R., Crowson, K., Schmidt, L., Kaczmarczyk, R., Jitsev, J.: LAION-5b: An open large-scale dataset for training next generation image-text models. In: *Thirty-sixth Conference on Neural Information Processing Systems Datasets and Benchmarks Track* (2022)
38. Sohl-Dickstein, J., Weiss, E., Maheswaranathan, N., Ganguli, S.: Deep unsupervised learning using nonequilibrium thermodynamics. In: Bach, F., Blei, D. (eds.)

- Proceedings of the 32nd International Conference on Machine Learning. Proceedings of Machine Learning Research, vol. 37, pp. 2256–2265. PMLR, Lille, France (07–09 Jul 2015)
39. Spanhol, F.A., Oliveira, L., Petitjean, C., Heutte, L.: A dataset for breast cancer histopathological image classification. *IEEE Transactions on Biomedical Engineering* **63**, 1455–1462 (2016)
 40. Tellez, D., Litjens, G., Bándi, P., Bulten, W., Bokhorst, J.M., Ciompi, F., Van Der Laak, J.: Quantifying the effects of data augmentation and stain color normalization in convolutional neural networks for computational pathology. *Medical image analysis* **58**, 101544 (2019)
 41. Thanh-Tung, H., Tran, T.: Catastrophic forgetting and mode collapse in gans. In: 2020 international joint conference on neural networks (ijcnn). pp. 1–10. IEEE (2020)
 42. Vahadane, A., Peng, T., Sethi, A., Albarqouni, S., Wang, L., Baust, M., Steiger, K., Schlitter, A.M., Esposito, I., Navab, N.: Structure-preserving color normalization and sparse stain separation for histological images. *IEEE transactions on medical imaging* **35**(8), 1962–1971 (2016)
 43. Vu, Q.D., Jewsbury, R., Graham, S., Jahanifar, M., Raza, S.E.A., Minhas, F., Bhalariao, A., Rajpoot, N.: Nuclear segmentation and classification: On color and compression generalization. In: International Workshop on Machine Learning in Medical Imaging. pp. 249–258. Springer (2022)
 44. Vu, Q.D., Rajpoot, K., Raza, S.E.A., Rajpoot, N.: Handcrafted histological transformer (h2t): Unsupervised representation of whole slide images. *Medical Image Analysis* **85**, 102743 (2023)
 45. Wang, R., Khurram, S.A., Walsh, H., Young, L.S., Rajpoot, N.: A novel deep learning algorithm for human papillomavirus infection prediction in head and neck cancers using routine histology images. *Modern Pathology* **36**(12), 100320 (2023)
 46. Wang, X., Yu, K., Wu, S., Gu, J., Liu, Y., Dong, C., Loy, C.C., Qiao, Y., Tang, X.: Esrgan: Enhanced super-resolution generative adversarial networks. In: ECCV Workshops (2018)
 47. Wang, Z., Bovik, A.C., Sheikh, H.R., Simoncelli, E.P.: Image quality assessment: from error visibility to structural similarity. *IEEE Transactions on Image Processing* **13**, 600–612 (2004)
 48. Weigert, M., Schmidt, U.: Nuclei segmentation and classification in histopathology images with stardist for the conic challenge 2022. arXiv preprint arXiv:2203.02284 (2022)
 49. Xu, K., Jahanifar, M., Graham, S., Rajpoot, N.: Accurate segmentation of nuclear instances using a double-stage neural network. In: Medical Imaging 2023: Digital and Computational Pathology. vol. 12471, pp. 506–515. SPIE (2023)
 50. Yellapragada, S., Graikos, A., Prasanna, P., Kurc, T., Saltz, J., Samaras, D.: Pathldm: Text conditioned latent diffusion model for histopathology. In: Proceedings of the IEEE/CVF Winter Conference on Applications of Computer Vision. pp. 5182–5191 (2024)
 51. Zhang, L., Rao, A., Agrawala, M.: Adding conditional control to text-to-image diffusion models. In: Proceedings of the IEEE/CVF International Conference on Computer Vision (ICCV). pp. 3836–3847 (October 2023)
 52. Zhang, W.: Conic solution. arXiv preprint arXiv:2203.03415 (2022)

Supplementary Material

A Preliminaries

A.1 Neural Style Transfer

To generate the training data we perform NST [9] with our sampled source set \mathbb{S} and target set \mathbb{T} . Specifically, we treat a given source image $p^s \in \mathbb{S}$ as the content image, a given target image $p^t \in \mathbb{T}$ as the style image and generate a stylized image $p_{s,t}^u$. At the start of the NST process, $p_{s,t}^u$ is a clone of the content image *i.e.* $p_{p^s, p^t}^u = p_i^s$ which is then refined by the NST process. Using a VGG16 pre-trained on ImageNet, denoted as \bar{F} , we extract features from every pooling layer in the network for all images creating three sets of features \bar{F}_s , \bar{F}_t and \bar{F}_u where $\bar{F}_i = \{\bar{f}^q, \forall q \in \{1, 2, \dots, n\}\}$ where n is the number of pooling layers in the VGG16 and f^q is the feature representation of image i at layer q .

Given \bar{F}_s , \bar{F}_t and \bar{F}_u we compute the mean squared loss between \bar{F}_s and \bar{F}_u feature-wise at each layer resulting in the overall content loss across all pooling layers

$$L_{content}(\bar{F}_s, \bar{F}_u) = \sum_0^n (\bar{F}_s - \bar{F}_u)^2. \quad (4)$$

The style loss is computed by calculating the Gram matrix G of the target image's features \bar{F}_t and the stylized image \bar{F}_u at each layer and computing the mean squared loss between these Gram matrices

$$L_{style}(\bar{F}_t, \bar{F}_u) = \sum_0^n (G(\bar{F}_t) - G(\bar{F}_u))^2. \quad (5)$$

The final overall loss is given by

$$L_{total} = \alpha L_{content} + \gamma L_{style}, \quad (6)$$

where α and γ are weighting constants.

We set α to be 1 and γ to be 10,000 for all of our work as this was found to lead to the best qualitative results. This loss is then backpropagated through the stylized image, p^u , for 300 iterations producing the final version of p^u . For a 1024^2 RGB image, this works out to be 3,145,728 parameters.

We use the Adam [19] optimizer and mixed precision to increase the data generation speed due to the significant computational cost of this process. By repeating this process for every pairing of every image in \mathbb{S} and \mathbb{T} we generate the corresponding set \mathbb{U} where every s_i has been transformed with the style of every t_j . In total this results in 2,097,152 images for training.

Additionally, we scale the matrix dot product operation in the gram matrix calculation G while using mixed precision to prevent float overflow error that occurs during the transition between fp16 and fp32. Empirically, we found that NST with fp16 provides the same image quality as NST with fp32, with an average cosine similarity of 0.999 across 10 image pairs. Using fp16 instead of 32 provides a speedup of 1.25 to 2 depending on the GPU used for NST.

A.2 Latent diffusion models

Latent diffusion models (LDMs) [28], like other DDPMs, consists of a forward and a reverse process. However, a distinctive feature of LDM is that it operates in the latent space, typically encoded via an AutoEncoder \mathcal{E} , instead of in the pixel space. This significantly improves the efficiency of the diffusion process. Therefore, LDM has been adopted in this study. The forward diffusion process of LDM is defined as a Markov chain which maps the sample from the real data distribution to a Gaussian distribution by gradually adding Gaussian noise to the sample. Let z_0 denote the encoded latent representation of the input image p , obtained by an AutoEncoder \mathcal{E} , such that $z_0 = \mathcal{E}(p)$; while z_t denote the noised version of z_0 at timestep t , the forward diffusion process $q(\cdot)$ is defined as

$$q(z_t|z_{t-1}) := \mathcal{N}(z_t; z_{t-1}\sqrt{1 - \beta_t}, \beta_t I), \quad (7)$$

where $\{\beta_t \in (0, 1)\}_{t=1}^T$ is the time scheduler and I is the identity matrix. The time scheduler β_t controls the amount of noise to be added to the sample z_{t-1} at timestep t . The reverse process aims to reconstruct the initial latent representation z_0 from z_T . This is achieved by training a time conditional model to estimate the conditional probability distribution to recover the latent representation z_{t-1} at timestep $t-1$ given z_t . In LDM, a time-conditional UNet [29] is used as the backbone network for such purpose. If β_t is small enough, $q(z_{t-1}|z_t)$ will also be a Gaussian distribution [38]. Therefore, the reverse process can be defined as

$$p_\theta(z_{t-1}|z_t) := \mathcal{N}(z_{t-1}; \mu_\theta(z_t, t), \Sigma_\theta(z_t, t)), \quad (8)$$

where $\mu_\theta(z_t, t)$ and $\Sigma_\theta(z_t, t)$ is the mean and the covariance of the Gaussian distribution determined by time t , latent z_t at timepoint t , and the learned model parameters θ .

B Model training

B.1 Implementation details

We use a Stable Diffusion v2.1 model [28] pre-trained on LAION-5B [37] as the backbone for our model⁵. We train StainFuser with AdamW [22] with a learning rate of $1e-5$ and weight decay of $1e-2$ for 3 epochs with an effective batch size of 32. Training the full model on 512^2 images with 512 target sets took 81 hours on 2 A100 GPUs with 16 images per GPU.

B.2 Sudden convergence phenomenon

In Zhang *et al.* [51], the authors reported a sudden convergence phenomenon during model training, which was also observed in our experiments. In the early

⁵ Backbone pre-training details are available at the model card: <https://huggingface.co/stabilityai/stable-diffusion-2-1-base>

training stage, the model can generate high-quality images with histological features, but they do not adhere to the guidance provided by the source image condition p^s . As shown in Figure A1, the model suddenly learned how to generate images based on the guidance from p^s after a certain number of optimization steps.

B.3 Decoder frozen vs. unfrozen during training

A large-scale training strategy was also proposed in Zhang *et al.* [51], which involves initially training only the conditioning component of the model for a large number of steps, and the entire model, including the stable diffusion component, is then trained jointly. Given our constraints in computational resources, we explored whether unlocking only the decoder part of the stable diffusion component could enhance training speed and convergence. Therefore, we trained two models: one with the frozen decoder and the other with the unfrozen decoder. We then observed the performance of each model on an unseen validation set at various optimization steps.

We report the results in Figure A1. We can see that the sudden convergence phenomenon appeared earlier on the model with a frozen decoder. However, after both models learned how to generate the morphological content based on p^s , the model with the unfrozen decoder generates images with a better stain and image quality. We hypothesize that because the model with a frozen decoder only needs to optimize its conditioner, it (StainFuser) therefore learns faster adherence to the guiding signal from p^s . However, once the model adheres to the signal p^s sufficiently, the one with a frozen decoder has trouble integrating the stain properties of p^t into the final output, thus achieving less desirable image quality compared to the one with an unfrozen decoder.

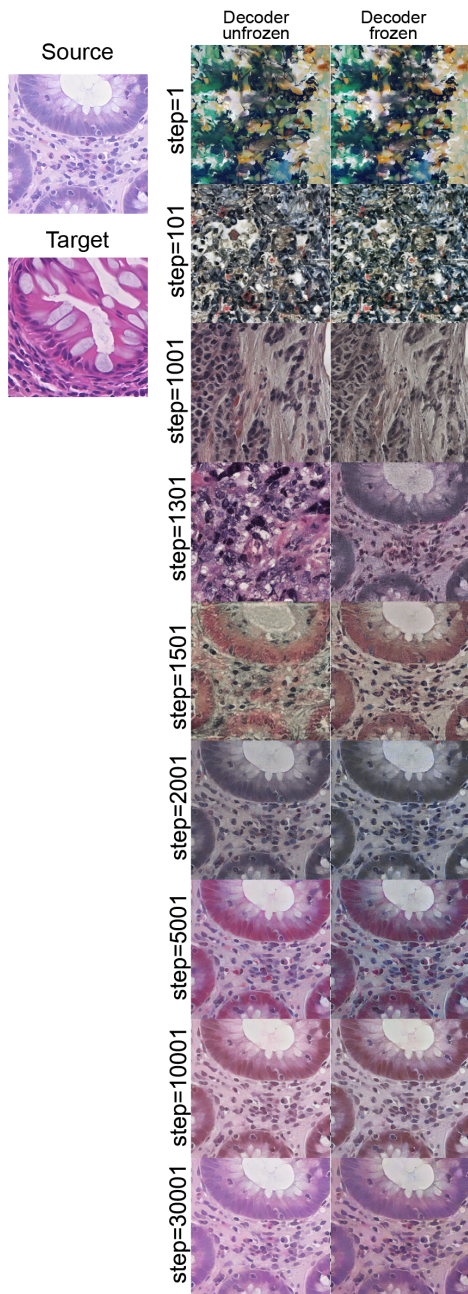


Fig. A1: Qualitative comparisons between decoder frozen and unfrozen during training shown in different optimization steps.

C Extended Experiment Design

We follow the study design of Vu *et al.* [43] and up-scaled the test data from CoNIC [11] with ESRGAN [46] super-resolution creating the **Control** set. These images were 1024^2 and used for NST as this has been shown to significantly improve the performance of NST [9, 43]. This **Control** set was used for all comparisons with the original data and resized back to 256^2 or 512^2 with bi-linear interpolation to make the comparisons between methods as fair as possible. For each method and experimental setting studied we normalized the entirety of the **Control** version of the test set *w.r.t.* each sampled target. *i.e.* for each sampled target we generate a new version of each image in the testing set where the given image has been normalized using the chosen method with respect to the specified target.

This process is designed to provide a robust evaluation of the stain normalization process, instead of assessing stain normalization methods for one target image only. Existing work has shown that, for example, Vahadane stain normalization can lead to a wide spread of performance downstream depending on what image target is chosen [43]. While the exact mechanism by which this variation arises has not been fully explored we believe the principle of assessing performance across a range of sampled targets provides a more thorough and representative evaluation of downstream performance compared to using one single target which can be cherry-picked easily.

C.1 Motivation

We further argue that assessing normalization methods on image-level tasks such as tumor or tissue classification is insufficient to fully assess the important capabilities of a stain normalization algorithm. Most of the publicly available datasets used for these tasks such as Kather100k [18] and BreakHis [39] are image-level classification tasks where each image is assigned one of n labels representing the class of the image such as tumor vs. non-tumor classification. It is relatively easy to achieve high performance on these image-level classification tasks using features that do not take account of local morphology, mean color for example. This implies that when assessing with a framework such as this a normalization method could theoretically disrupt the local morphology of the original image and still achieve superior performance compared to a baseline because it aligns the unseen sample better to the features (abstract or not) a model has learned. This would be potentially disastrous in clinical applications where the local morphology of nuclei is highly significant for many clinical tasks. Instance-level nuclei segmentation tasks like CoNIC, however, do not suffer from this issue. If a normalization method perturbs the original morphology during the style transfer process either a downstream model will not be able to detect a given nucleus, missing the instance, or it will segment the distorted nucleus resulting in a contour boundary with poor intersection compared to the ground truth mask and thus panoptic segmentation metrics will penalize this accordingly, provided the downstream model has good performance. Prior work [43]

has shown modern nuclei instance segmentation and classification models are robust regarding compression artifacts; as such we argue they are suitable for this task.

D Ablation Study

D.1 Importance of Image Resolution.

We study the impact of image resolution by training StainFuser on two different image resolutions 512^2 and 256^2 . These resolutions are the two most common resolutions for inference in CPath WSI-level work and thus allow us to explore whether a higher resolution is required for good performance. We utilized the PathAI model for evaluating the impacts of the resolution on the downstream task.

The quantitative results are reported in Table A1 and additional qualitative examples are provided in Figure A2. From these results, we find that the higher resolution of 512^2 images is crucial for both image quality and downstream performance. The StainFuser model trained on 512^2 images drastically outperforms the model trained on 256^2 images whether applied on 256^2 or 512^2 as shown in Table A1. Furthermore, the 246^2 trained model’s performance improves when applied on 512^2 images both in terms of image quality and downstream performance.

We hypothesize this is likely due to the frozen VAE we use in our architecture. This VAE was originally trained on 512^2 images and as such likely has learned feature embeddings for pixel arrangements only found in images of this resolution or larger. As such when it is used to embed smaller images the embeddings do not contain sufficiently high-quality information for StainFuser to learn and apply the style transfer effectively.

Lastly, the improved performance of StainFuser at 512^2 compared to 256^2 also has positive connotations for downstream application at the WSI level as by normalizing at this resolution the number of tiles in a WSI that need to be processed is reduced by a factor of 4 providing significant computational speedup.

We use models trained on 512^2 images for all other ablations due to the difference in downstream performance observed here.

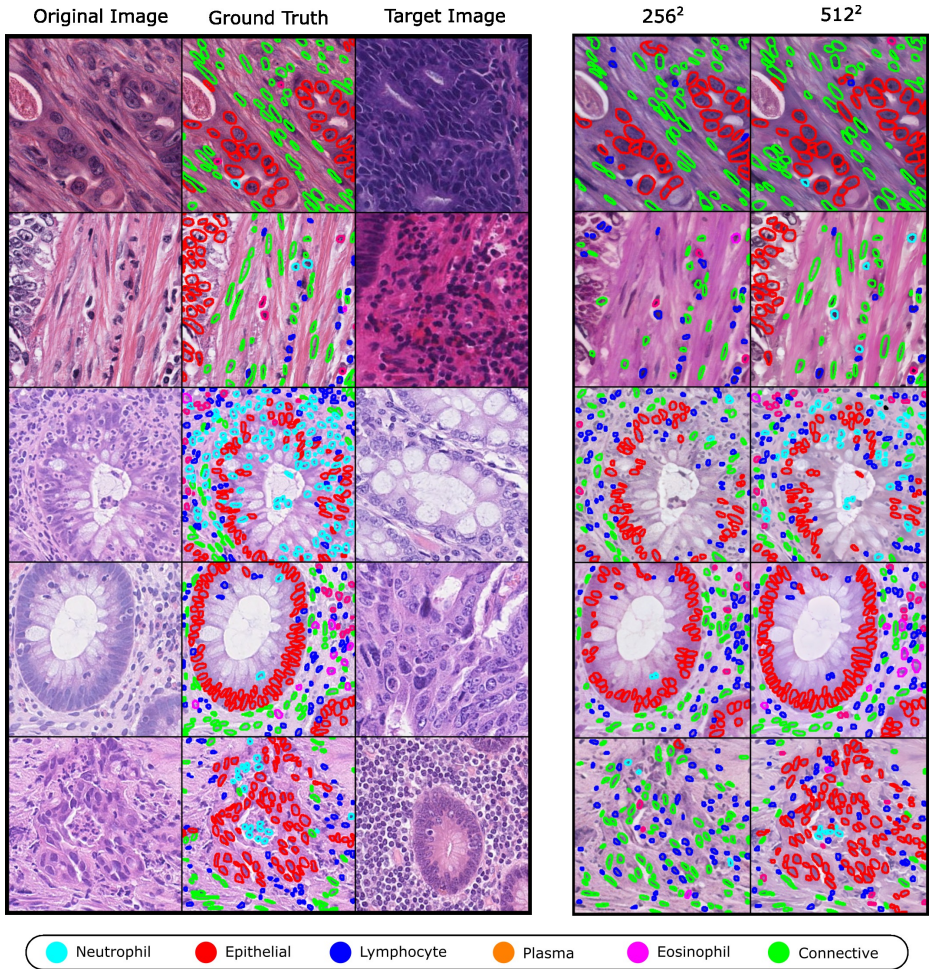


Fig. A2: Qualitative results showing the influence of image resolution for downstream performance. We observe that the normalized images generated by StainFuser trained at 256² can lead to the misclassification of nuclei (bottom row) and missed nuclei (second and third row). All predictions are using the PathAI model.

Table A1: Results for different image resolutions during training and inference. We train 2 models, 1 on 256^2 data and 1 on 512^2 data and then apply each on 256^2 and 512^2 unseen data observing that the larger resolution of 512^2 data leads to better performance even when the model was trained on 256^2 images. Best performance is highlighted in blue.

Resolution		$mPQ^+AUC \uparrow$	FID \uparrow	PSNR \uparrow	SSIM \uparrow
Training	Inference				
256^2	256^2	0.100 ± 0.003	79.270 ± 7.238	19.827 ± 0.999	0.607 ± 0.008
512^2	256^2	0.117 ± 0.004	59.328 ± 6.663	20.014 ± 0.941	0.612 ± 0.009
256^2	512^2	0.157 ± 0.006	40.164 ± 7.408	21.814 ± 1.036	0.808 ± 0.013
512^2	512^2	0.214 ± 0.011	32.760 ± 10.398	23.777 ± 1.090	0.868 ± 0.017

Table A2: Effect of image magnification during training on generated image quality and downstream performance. We trained 3 different models each with all 512 target sets at 512^2 resolution. Best results are highlighted in blue.

Magnification	$mPQ^+AUC \uparrow$	FID \uparrow	PSNR \uparrow	SSIM \uparrow
20x	0.214 ± 0.011	32.760 ± 10.398	23.777 ± 1.090	0.868 ± 0.017
40x	0.209 ± 0.008	28.878 ± 7.718	22.585 ± 0.815	0.836 ± 0.008
20x & 40x	0.215 ± 0.007	25.882 ± 8.233	23.911 ± 0.816	0.875 ± 0.010

D.2 Image Magnification.

We study the impact of image magnification by training StainFuser models on images with magnifications of 20x, 40x and a mixture of 20x and 40x during training. Similarly, we utilized PathAI model for evaluating downstream performance. Our results are included in Table A2.

In the mixed image setting when a sample is fetched from the dataloader we randomly select a sample with probability 0.5, either a 40x or a 20x version of the same image, target pair at the given fixed image resolution *i.e.* 512^2 . We find that models trained on 20x data marginally outperform those trained on 40x data in terms of PSNR and SSIM but not in FID.

In terms of downstream performance, the PathAI model performed marginally better with the 20x StainFuser data ($+0.005 mPQ^+AUC$) compared to the 40x StainFuser data across the normalized test sets. Additionally, the StainFuser trained using 20x and 40x data outperforms both other training settings in terms of image quality, across FID, PSNR and SSIM, and in terms of downstream mPQ^+AUC . This is potentially due to the distribution of image magnifications within the CoNIC test set where the majority of the images were captured at 20x magnification. By extension, the 20x and 40x model benefits by seeing all the magnifications within the testing set and our results show this is both in terms of image quality and downstream performance. Given this, we expect the 20x

and 40x model to generalize better than the other models to other downstream tasks having been exposed to both magnifications in training.

D.3 Data Volume.

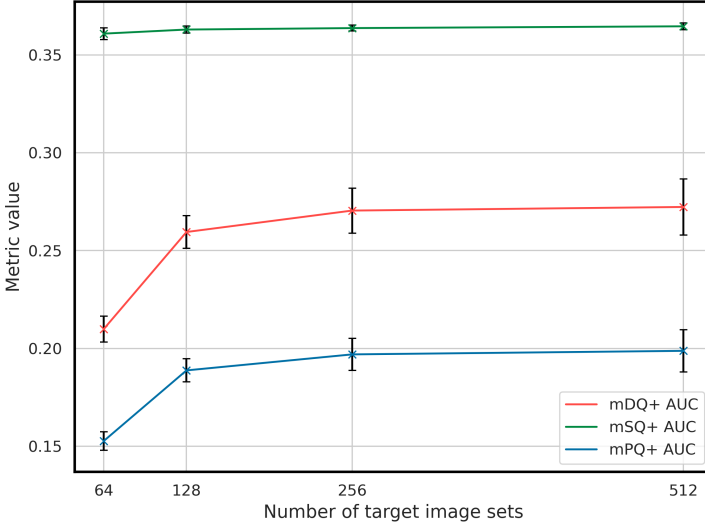


Fig. A3: Graph of how PathAI’s performance in terms of mDQ^+AUC , mSQ^+AUC and mPQ^+AUC are affected by the volume of data used in StainFuser’s pretraining. Error bars indicate the standard deviation across all targets sets for each metric. Results are from model trained at 512^2 resolution and 20x magnification.

We train 4 different StainFusers using a different number of target sets to explore the importance of the amount of our sampled training data on performance. Similarly, we utilized the PathAI model for evaluating downstream performance. Specifically, we use 64, 128, 256 and 512 target sets for our ablations. The target sets are chosen by sampling from the color distribution of the reference image of the given target set to encompass as much of the overall color space as possible. Furthermore, as the number of target sets increases the higher number always includes all of the previous target sets. *i.e.* the target sets in the 128 experiment contain all the target sets of the 64 experiment in addition to 64 others *etc.* These target set numbers correspond to 262,144, 524,288, 1,048,576 and 2,097,152 unique images in each training set respectively.

We report the results in Table A3. Here, we observe that the more data used for training the higher quality images StainFuser generates on unseen data and the better the PathAI model performs on the corresponding normalized test datasets. We plot how much the performance changes *w.r.t.* the training volume in Figure A3. Here, we see the performance improvement is much steeper when

Table A3: Comparison between StainFuser models trained with different volumes of data. Models are trained for 3 epochs at 512^2 resolution, at 20x magnification. mPQ^+AUC results are using the PathAI model

Target Sets	$mPQ^+AUC \uparrow$	FID \uparrow	PSNR \uparrow	SSIM \uparrow
64	0.168 ± 0.005	44.951 ± 8.836	19.304 ± 0.576	0.797 ± 0.010
128	0.204 ± 0.006	39.541 ± 11.062	21.648 ± 0.901	0.821 ± 0.010
256	0.212 ± 0.008	36.391 ± 10.602	21.836 ± 0.976	0.827 ± 0.014
512	0.214 ± 0.011	32.760 ± 10.398	23.777 ± 1.090	0.868 ± 0.017

going from 64 to 128 target sets. However, beyond this point the improvements slowly plateau.

On the whole, it is clear that unsurprisingly the more diverse data StainFuser is trained on the higher quality images it generates and the better downstream models using its normalised data perform.

E WSI inference

The model used for StainFuser was trained on 512 target set using patches extracted at both $20\times$ and $40\times$ magnification level with image size of 512^2 . For inference, images were processed at $20\times$ magnification with image size of 512^2 , and StainFuser’s denoising step was set to 20. CAGAN inference was performed with the model trained on TCGA-IDH [21] dataset, as detailed in the study [6]. We used TIAToolbox’s [25] implementation for Vahadane method. Only tissue sections were processed. Two different slides were selected which come from two different anatomic sites (*i.e.* head and neck, colon). Two target images were chosen from two different slides unseen to the StainFuser model. **Target#1** was selected from slide

TCGA-4P-AA8J-01Z-00-DX1.5B44796F-D099-4076-9CAF-B40C2B83F432, and

Target#2 was selected from the slide

TCGA-QK-AA3J-01Z-00-DX1.ABCA519E-CF09-4FB3-812F-A977C4F0BA91.

F Additional Illustrative Results

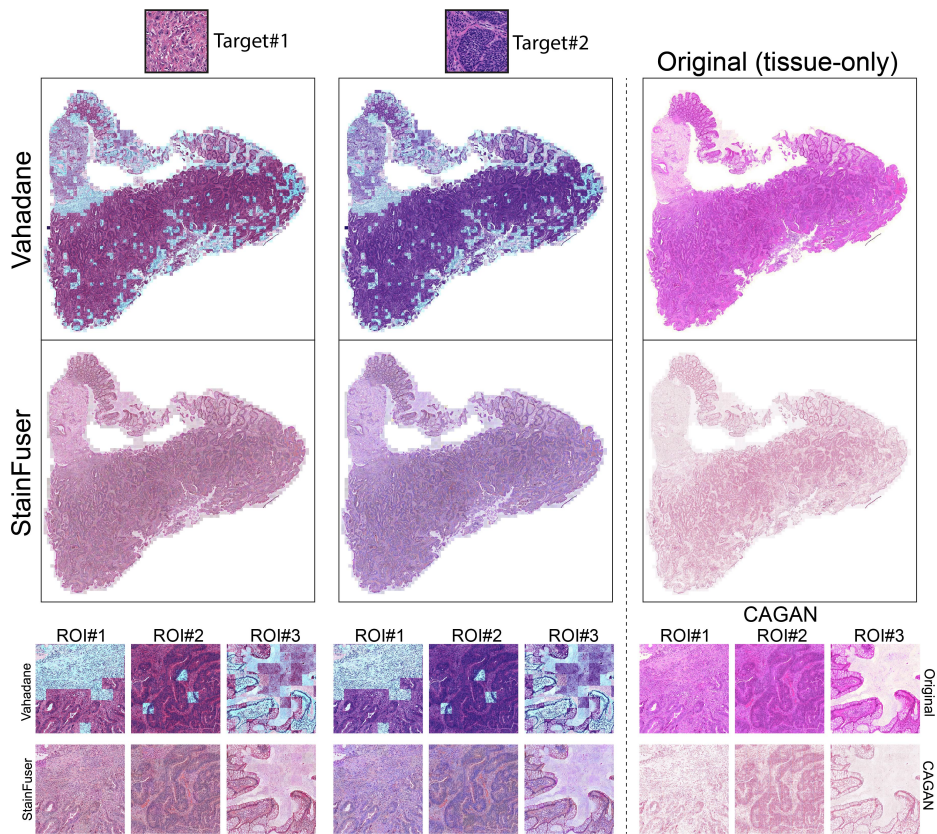


Fig. A4: WSI inference comparison between Vahadane, StainFuser and CAGAN. The slide was chosen from TCGA-COAD and 2 target images were chosen from 2 different unseen slides to the StainFuser.

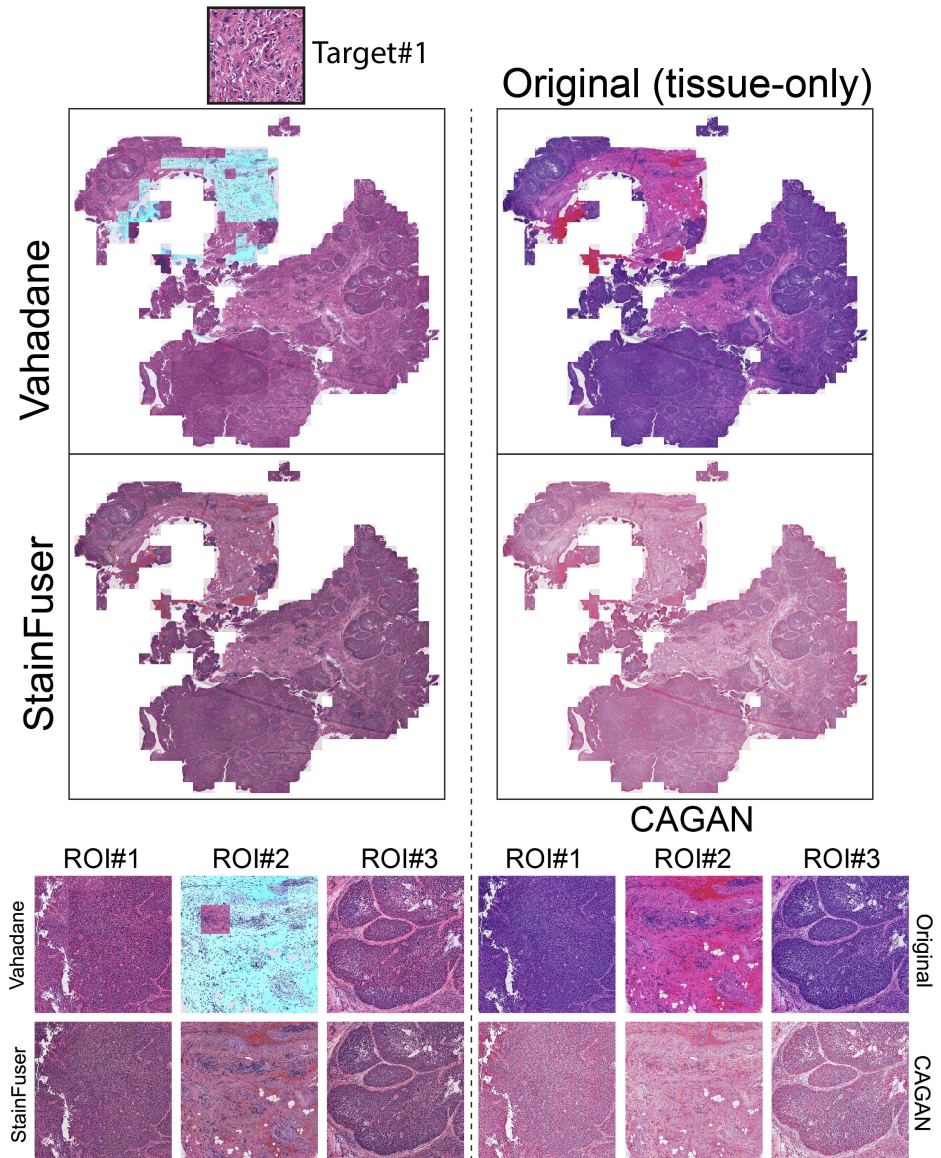


Fig. A5: WSI inference comparison between Vahadane, StainFuser and CAGAN. The slide was chosen from TCGA-HNSC and 1 target image was chosen from 1 unseen slide to the StainFuser.

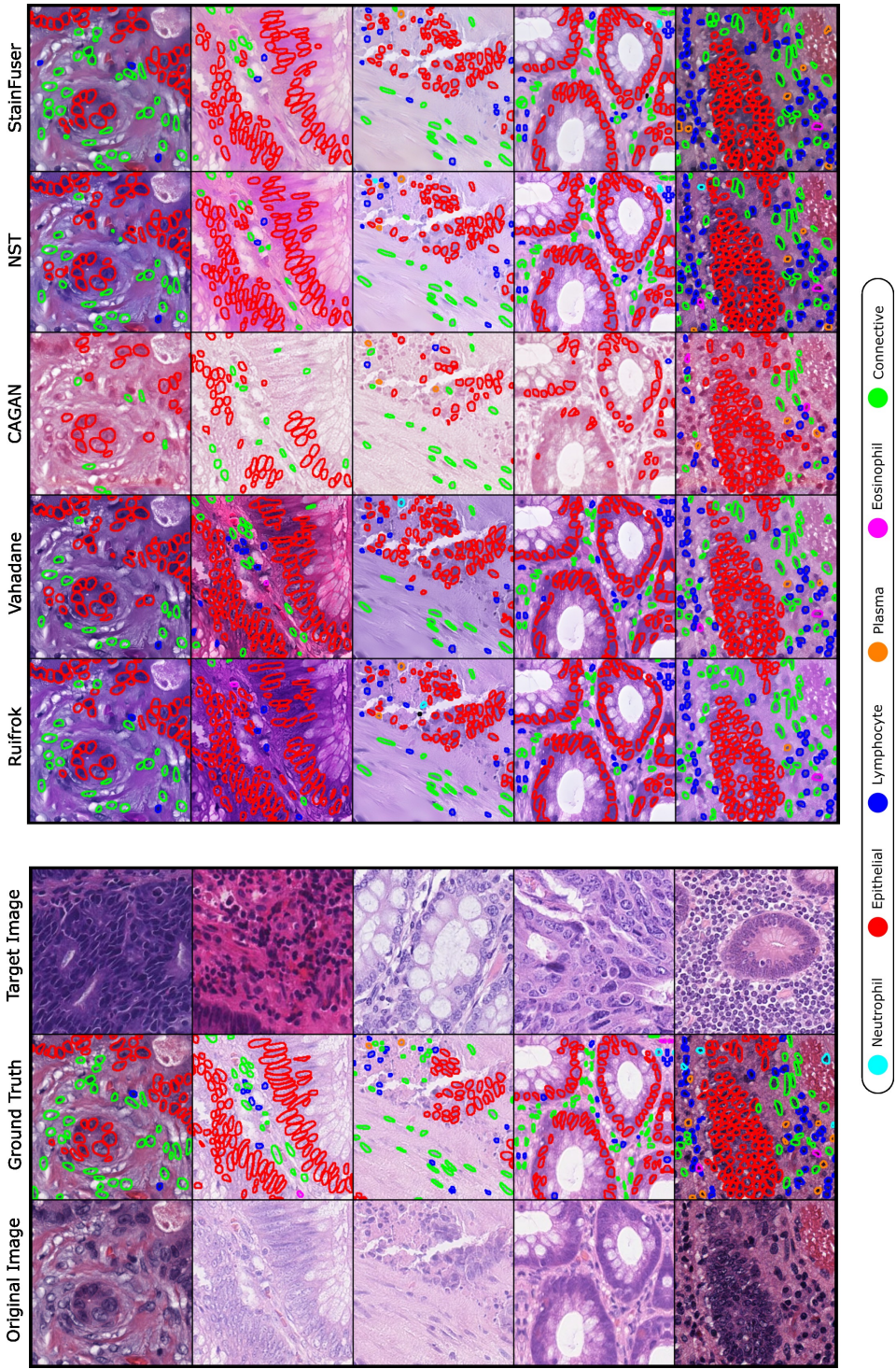


Fig. A6: Qualitative results of PathAI model applied on each normalization method

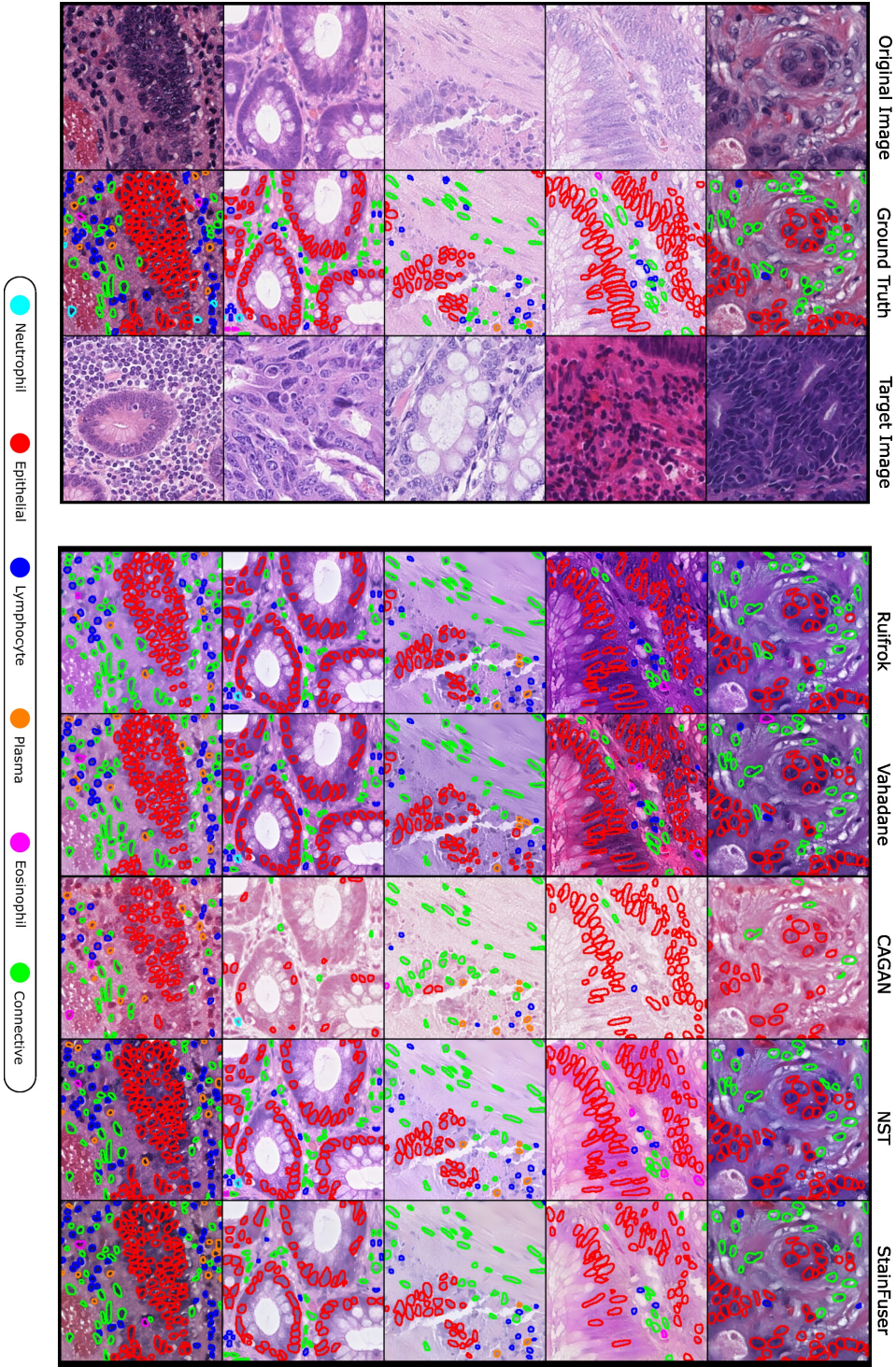


Fig. A7: Qualitative results of Bern model applied on each normalization method

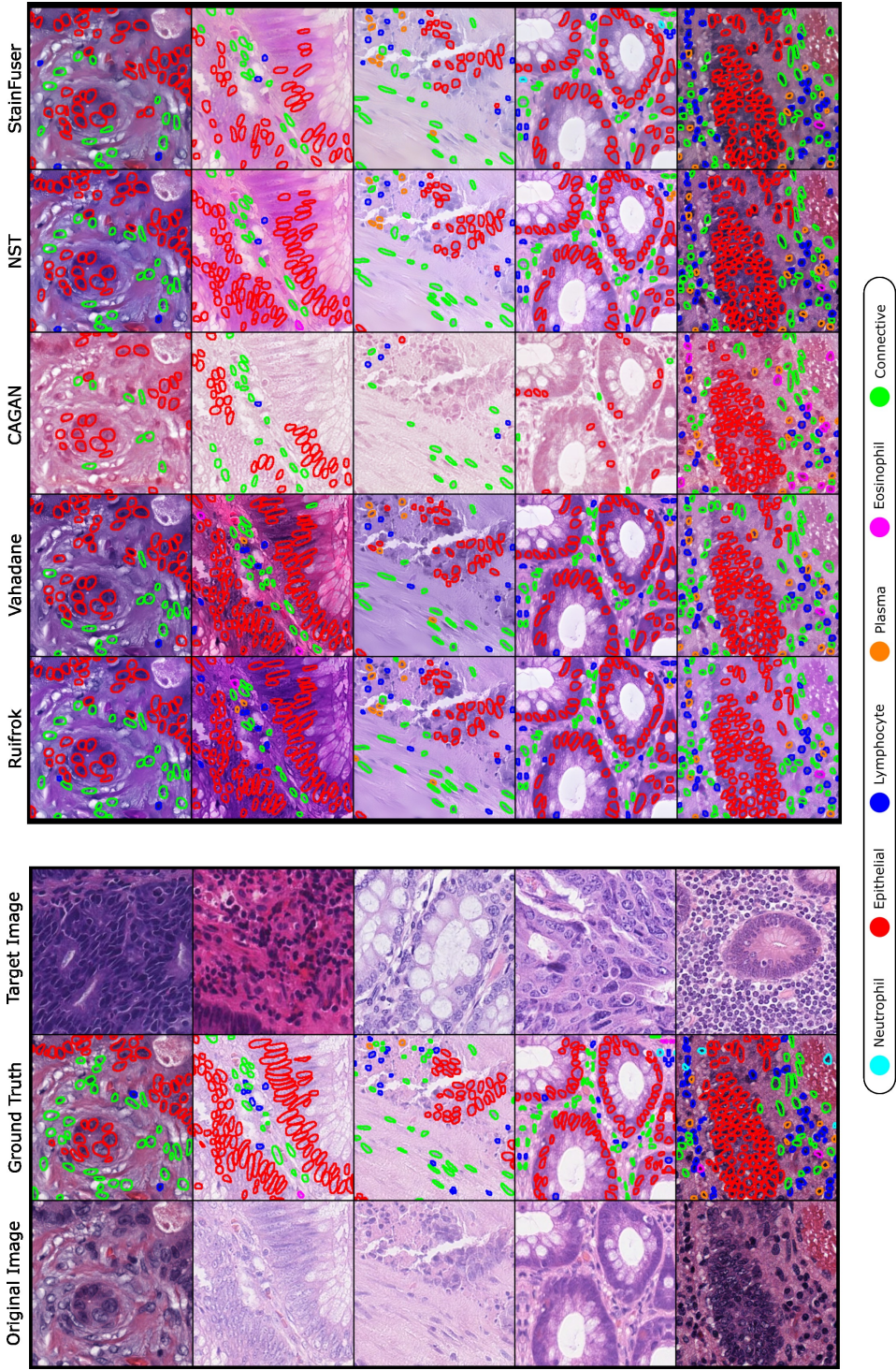


Fig. A8: Qualitative results of StarDist model applied on each normalization method

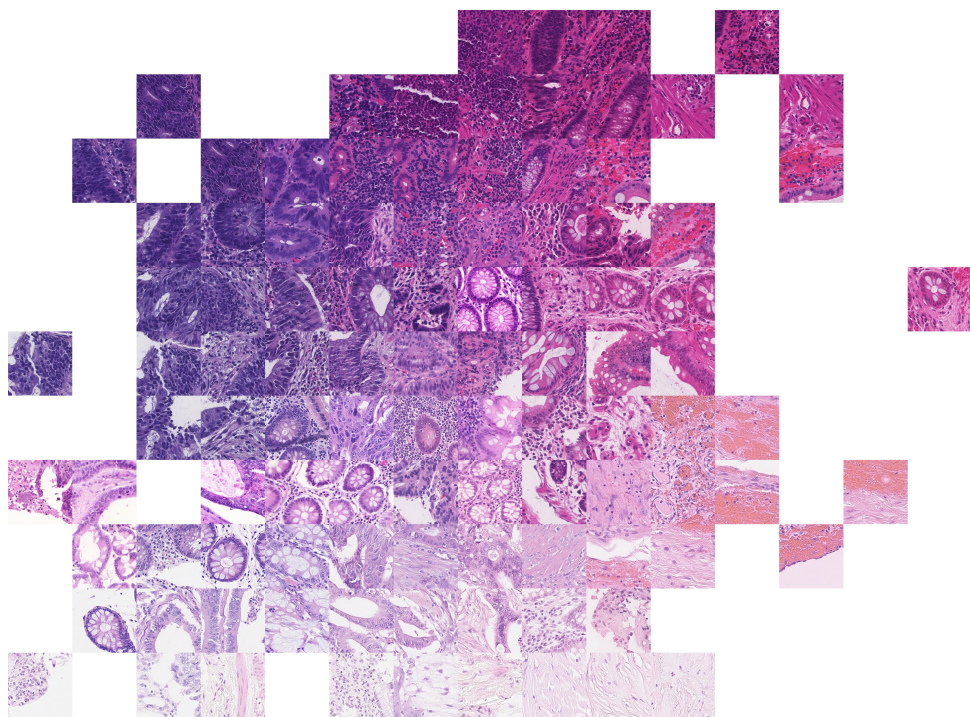


Fig. A9: High-resolution version of sampled references

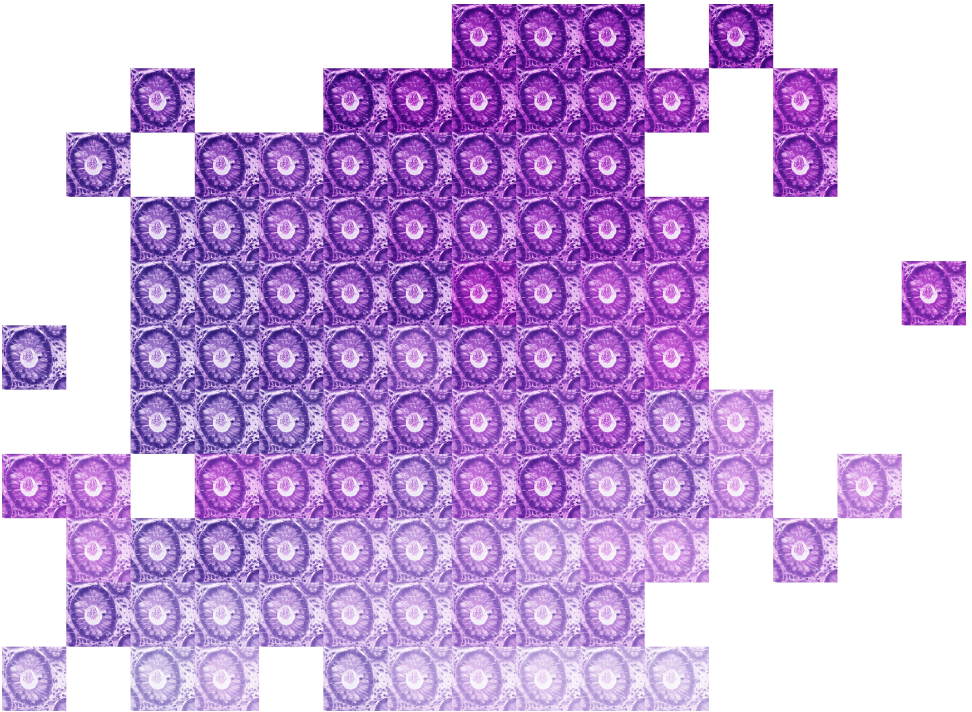


Fig. A10: High-resolution version of image normalised by Ruifrok [30] with respect to references in Figure A9

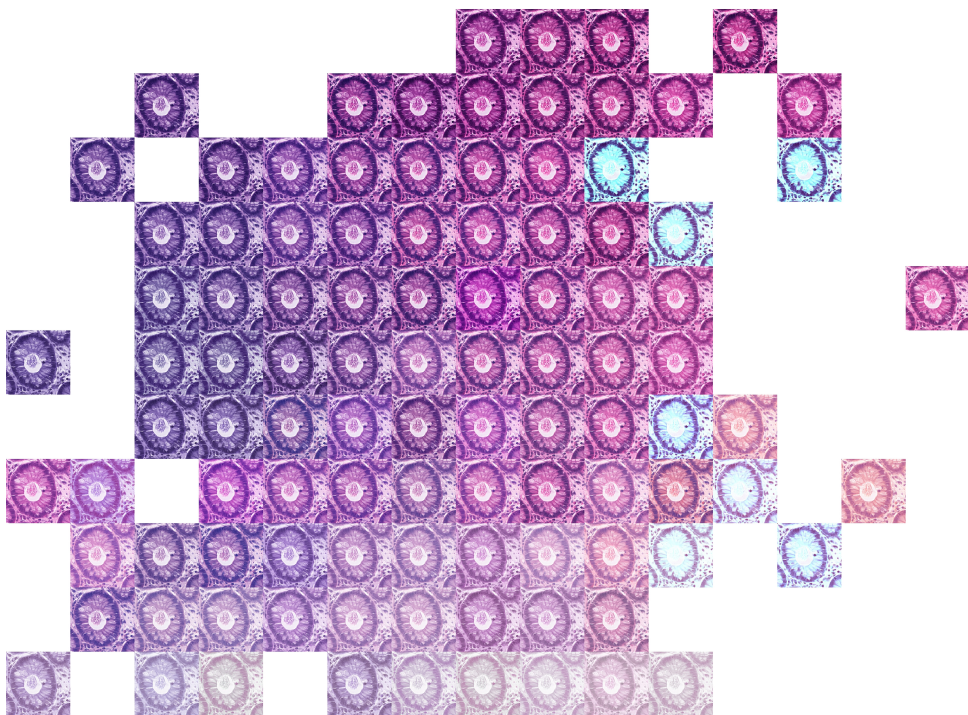


Fig. A11: High-resolution version of image normalised by Vahadane [42] with respect to references in Figure A9

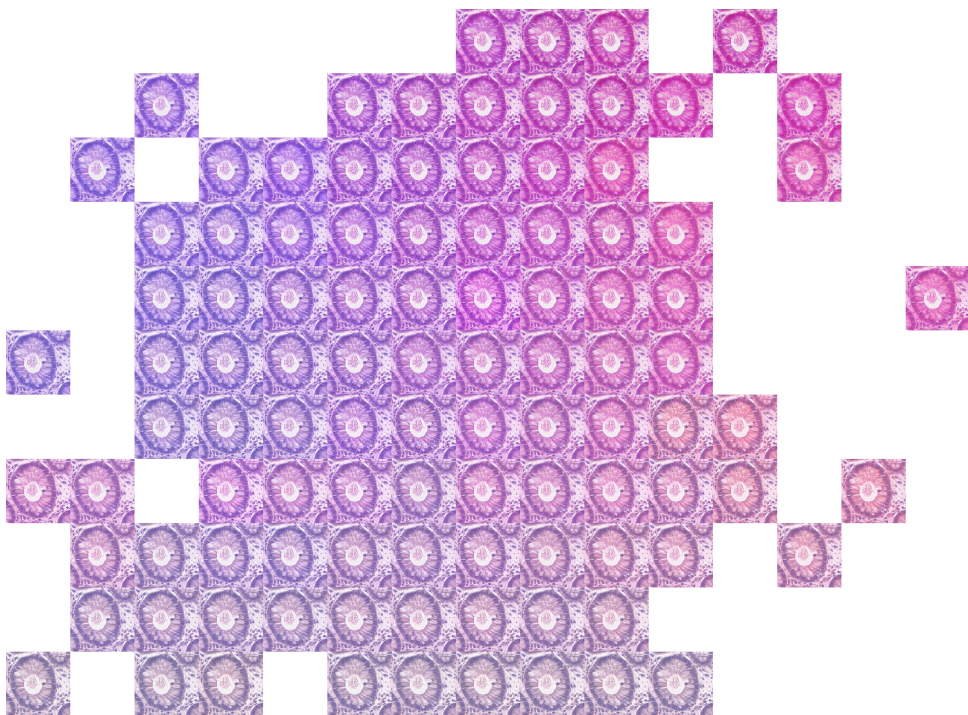


Fig. A12: High-resolution version of image normalised by NST [9] with respect to references in Figure A9

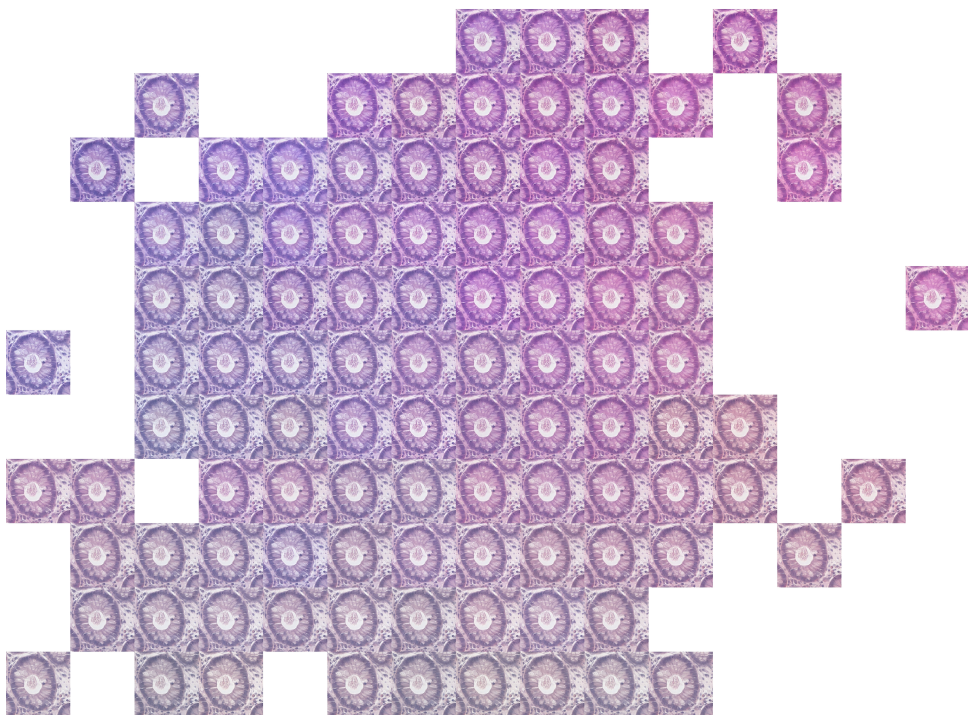


Fig. A13: High-resolution version of image normalized by StainFuser with respect to references in Figure A9